THESIS FOR THE DEGREE OF DOCTOR OF TECHNOLOGY

Functional Oxide Materials exhibiting Ionic Conductivity for Future Energy Conversion Needs

Synthesis, Characterization and Structure-Property Relationships

FRANCIS G.KINYANJUI

Department of Chemical and Biological Engineering

CHALMERS UNIVERSITY OF TECHNOLOGY

Göteborg, Sweden 2013

Functional Oxide Materials exhibiting Ionic Conductivity for Future Energy Conversion Needs

Synthesis, Characterization and Structure-Property Relationships

FRANCIS G. KINYANJUI

ISBN: 978-91-7385-884-7

Doktorsavhandlingar vid Chalmers tekniska högskola

Ny serie nr: 3565

ISSN: 0346-718X

Department of Chemical and Biological Engineering
Chalmers University of Technology
SE-412 96 Göteborg
Sweden
Telephone + 46 (0)31-772 1000

Cover: Representations of the pyrochlore (left) and perovskite (right) structures.

Reprint

Printed at Chalmers Reproservice AB

Göteborg, Sweden 2013

To my Wife and Family

”Mgaagaa na upwa hali wali mkavu”.

A swahili proverb

ABSTRACT

Fuel cells are electrochemical devices that transform the chemical energy in hydrogen and oxygen into electrical energy at high efficiencies and produce only water vapour emissions. Materials with the perovskite or fluorite structure types are commonly employed as the ion conducting ceramic electrolyte membranes in intermediate and high temperature fuel cells. However, due to the desire for lower operating temperatures of ~ 600 °C, there exists several challenges, namely: i) insufficient ionic conductivity (minimum required ~ 10^{-2} Scm^{-1}), ii) poor densification and iii) poor conductivity across grain boundaries. Another problem for proton conducting ceramic fuel cells is the lack of suitable cathode materials with appropriate mixed protonic-electronic conduction. In-situ cells to characterize these materials with concurrent techniques are also not available. The works herein try to address these challenges by exploring the structure property interplay of several candidate materials. The main techniques used were: Thermogravimetric Analysis, powder X-ray and neutron diffraction and electrochemical impedance spectroscopy.

The proton conductivity of In^{3+}-$BaZrO_3$ was improved through co-doping with Yb^{3+} compared to individually doped In^{3+}-$BaZrO_3$ and Yb^{3+}-$BaZrO_3$ samples. Spark plasma sintering of In^{3+}-$BaZrO_3$ achieved high densities (92 %) samples, and the grain boundary conductivity was boosted in comparison to conventionally sintered samples. The oxygen deficient perovskite system, $Ba_3In_2ZrO_8$, substituted with Ga^{3+} and Y^{3+} and Gd^{3+} and Y^{3+} combinations was shown to posses' mixed ionic-electronic conduction with the Ga^{3+} containing sample having the greatest electron hole contribution. The crystal structure and conductivity of an alternative system to $BaZrO_3$, Sc^{3+} substituted $BaSnO_3$, was explored and $BaSn_{0.6}Sc_{0.4}O_{3-\delta}$ found to have a proton conductivity as high as the current leading materials, i.e., 1.07×10^{-3} S cm^{-1} at 600 °C. Disorder in the anion sub-lattice of the pyrochlore-fluorite, $Y_2(Ti_{1-x}Zr_x)_2O_7$ system, studied using advanced analysis of neutron diffraction data, was found to significantly enhance O^{2-} ion conductivity; in comparison disorder in the cation sub-lattice did not greatly influence the conductivity.

This work also demonstrates two cells developed for in-situ conductivity and hydration studies coupled to neutron diffraction using In^{3+}-$BaZrO_3$ samples, and new insights into the hydration behaviour with respect to temperature and the thermal parameters of the oxygen anions were gained.

Keywords: proton conduction, perovskites, oxygen deficient perovskites, neutron diffraction, *in-situ* cells, Rietveld refinements, deuteron position, $BaSnO_3$, $BaZrO_3$, $Ba_3In_2ZrO_8$

List of Abbreviations

TGA	Thermogravimetric analysis
XRPD	X-ray powder diffraction
NPD	neutron powder diffraction
SOFC	solid oxide fuel cells
PCFC	proton conducting fuel cells
EIS	Electrochemical Impedance Spectroscopy
σ	Conductivity ($\mathrm{S\ cm^{-1}}$)
Ea	activation energy
p	partial pressure of a gas e.g., (p (O_2) , p (H_2O))
SEM	Scanning Electron Microscopy

List of publications

This thesis is based on papers and manuscripts listed below.

I. Ahmed, F. G. Kinyanjui, S. M. H. Rahman, P. Steegstra, S. G. Eriksson, and E. Ahlberg, "Proton conductivity in mixed b-site doped perovskite oxide $BaZr_{0.5}In_{0.25}Yb_{0.25}O_{3-\delta}$," *Journal of The Electrochemical Society,* vol. **157**, pp. B1819-B1824, **2010**.

II. Ahmed, F. G. Kinyanjui, P. Steegstra, Z. J. Shen, S. G. Eriksson, and M. Nygren, "Improved proton conductivity in spark-plasma sintered dense ceramic $BaZr_{0.5}$ $In_{0.5}$ $O_{3-\delta}$," *Electrochemical and Solid-State Letters,* vol. **13**, pp. B130-B134, **2010**.

III. F. G. Kinyanjui, S. T. Norberg, I. Ahmed, S. G. Eriksson, and S. Hull, "In-situ conductivity and hydration studies of proton conductors using neutron powder diffraction," *Solid State Ionics,* vol. **225**, pp. 312-316, **2012**.

IV. S. T. Norberg, S. Hull, S. G. Eriksson, I. Ahmed, F. Kinyanjui, and J. J. Biendicho, "Pyrochlore to Fluorite Transition: The $Y_2(Ti_{1-x}Zr_x)_2O_7$ $(0.0 \leq x \leq 1.0)$ System," *Chemistry of Materials,* vol. **24**, pp. 4294-4300, **2012**.

V. F. G. Kinyanjui, S. T. Norberg, C.S. Knee and S. G. Eriksson "Proton conduction in oxygen deficient perovskite $Ba_3In_{1.4}Y_{0.3}M_{0.3}ZrO_8$ ($M = Ga^{3+}$ or Gd^{3+}) electrolytes," *Manuscript in preparation.*

VI. F. G. Kinyanjui, S. T. Norberg, C.S. Knee, I. Ahmed, S. Hull, L. Buannic, F. Blanc, C. P. Grey and S. G. Eriksson " Conductivity of $BaSn_{0.6}Sc_{0.4}O_{3-\delta}$ and the location of the deuteron site by neutron powder diffraction" *Manuscript in preparation.*

My contributions to the papers in the order above

i.) Synthesis, data collection for XRPD, TGA, EIS and SEM, data analysis for XRPD and TGA.

ii.) Synthesis, data collection for XRPD, TGA, EIS, and SEM/EDS. Contributed to writing of manuscript.

iii.) Synthesis, data collection for all methods, data analysis for EIS, testing of cells, sensor testing and writing of the paper.

iv.) Syntheses, data collection for XRPD and EIS, analysis of some of the EIS data.

v.) Syntheses, data collection and analysis of all data, writing of the paper.

vi.) Syntheses, data collection and analysis of all data except NMR and writing of the paper.

Contents:

Table of Figures

1. Introduction

When the industrial revolution begun, the world's population was estimated to be 700 million persons. It is projected that by the middle of this century it would grow to 9 billion [1] bringing with it an explosive growth in energy demand. During this time the main source of energy has been, and continues to be, hydrocarbon based, with coal and petroleum sources dominating. The problem with this is that these energy sources are non-renewable, and their reserves on the planet are a fixed amount. As the reserves get depleted, the prices are bound to rise. Therefore there is a need to efficiently use the remaining reserves and to also switch to renewable sources such as wind and solar. Even though wind and solar sources are unpredictable, when available in plenty they can be stored in chemical form (hydrogen) or in electrochemical form (batteries) for later use.

Fuel cells are electrochemical devices capable of continuously converting the chemical energy in a fuel such as hydrogen or methane to electricity after a chemical reaction with an oxidizing agent. William R. Grove demonstrated the basis of the fuel cell over a century and a half ago using the "Grove Cell" consisting of a zinc anode in sulphuric acid and a platinum cathode in nitric acid separated by a porous ceramic whereby the application of an electrical potential across its electrodes produced oxygen and hydrogen gases. The birth of the fuel cell concept came about by the realization that by removing the DC power source connected to the cell, the traces of gas bubbles on the electrodes produced a weak electrical signal across the electrodes.

Francis Thomas Bacon (1904-1992, British) first demonstrated a practical 5kW fuel cell system using potassium hydroxide as the electrolyte. In the same period across the Atlantic, Harry Karl Ihlrig rigged up a modified 15kW stack, consisting of

1,008 Bacon cells, onto an agricultural tractor manufactured by Allis-Chalmers capable of hauling 1.36 tonnes. With the backing of the US Air Force, the tractor makers went ahead to develop a submersible vessel, a forklift truck and a golf cart all powered by the alkaline fuel cell. Union Carbide in the late 1950's and in the 1960's demonstrated fuel cell powered mobile radar set for the US Army and also a fuel cell powered motorbike [2, 3].

In the early 1960's Pratt & Whitney brought fuel cells to the space age when they won a contract to power the Apollo spacecraft with alkali fuel cells, which were developed to provide electric power and drinking water for the astronauts. Fuel cells were later used to power space shuttle missions [2, 3].

Among the companies that have successfully commercialized fuel cells are UTC Power (PureCell 400 system, based on phosphoric acid) [4], Ballard (FCgen, ClearGen) [5], Siemens-Westinghouse and recently Bloom Energy (Bloom Energy server, based on a solid oxide fuel cell) [6].

Unlike petrol/diesel generators that first convert chemical energy to kinetic energy then to mechanical before arriving at electrical energy, fuel cells directly convert chemical energy to electrical energy. Through this direct conversion of chemical energy to electrical energy without any thermo-mechanical step, fuel cells are able to achieve large efficiencies in the conversion. Efficiencies of up to 60% are often achieved while efficiencies of roughly 80% can be achieved for the high temperature fuel cells in combined heat and power (CHP) setups [7-9]. Fuel cells additionally offer fewer greenhouse emissions [10] and lower noise pollution in comparison to diesel generators. There are various types of fuel cells classed according to the electrolyte material used, temperature of operation or mode of operation [11].

The electrolyte, at the heart of the fuel cell, is a membrane whose function is to allow the passage of ions such as H^+, O^{2-} or CO_3^{-2} through it whilst blocking both gas diffusion and electron. From a practical application view for commercialization, a membrane needs to have an electrical conductivity of at least 10^{-2} S cm^{-1} [12].

2. Fuel Cell Technologies

2.1 PEMs

Polymer electrolyte membrane (PEM) fuel cells have a solid, proton (H^+) conducting polymer, commonly Nafion by DuPont ($C_7HF_{13}O_5S{\cdot}C_2F_4$), as the electrolyte and operate at low temperatures ~ 80 °C. Typically they require a platinum catalyst that splits the hydrogen. The platinum catalyst is susceptible to carbon monoxide poisoning apart from being rather expensive and in limited supply. The fuel cells are light and hence easily applied in mobile applications such as electrically powered vehicles.

Anode Reaction: $2H_2 \rightarrow 4H^+ + 4e^-$ (over Pt Catalyst)

Cathode Reaction: $O_2 + 4H^+ + 4e^- \rightarrow 2H_2O$

Overall Cell Reaction: $2H_2 + O_2 \rightarrow 2H_2O$

2.2 SOFCs

Solid oxide fuel cells (SOFCs) have an electrolyte based on ceramic materials such as yttria-stabilized zirconia (YSZ) [13, 14], that conducts O^{2-} (the charge carriers), and operate at high temperatures (~700 °C). They can be deployed in a co-generation setup with turbines to achieve efficiencies of > 60% LHV (Lower Heat Value calculations assumes all water exhausted at the end of a fuel cell reaction is in the vapour form) [7]. Their high operating temperatures enable the use of different fuel types such as methane, hydrocarbon based fuels and even CO.

Anode Reaction: $2H_2 + 2O^{2-} \rightarrow 2H_2O + 4e^-$

Cathode Reaction: $O_2 + 4e^- \rightarrow 2O^{2-}$

Overall Cell Reaction: $2H_2 + O_2 \rightarrow 2H_2O$

The schematic of the SOFC using $H_{2\,(g)}$ fuel is illustrated in figure 1. It should be noted that on the anode side, the H_2O produced dilutes the incoming fuel feed and the exhaust gas has to be separated to recover the unspent fuel.

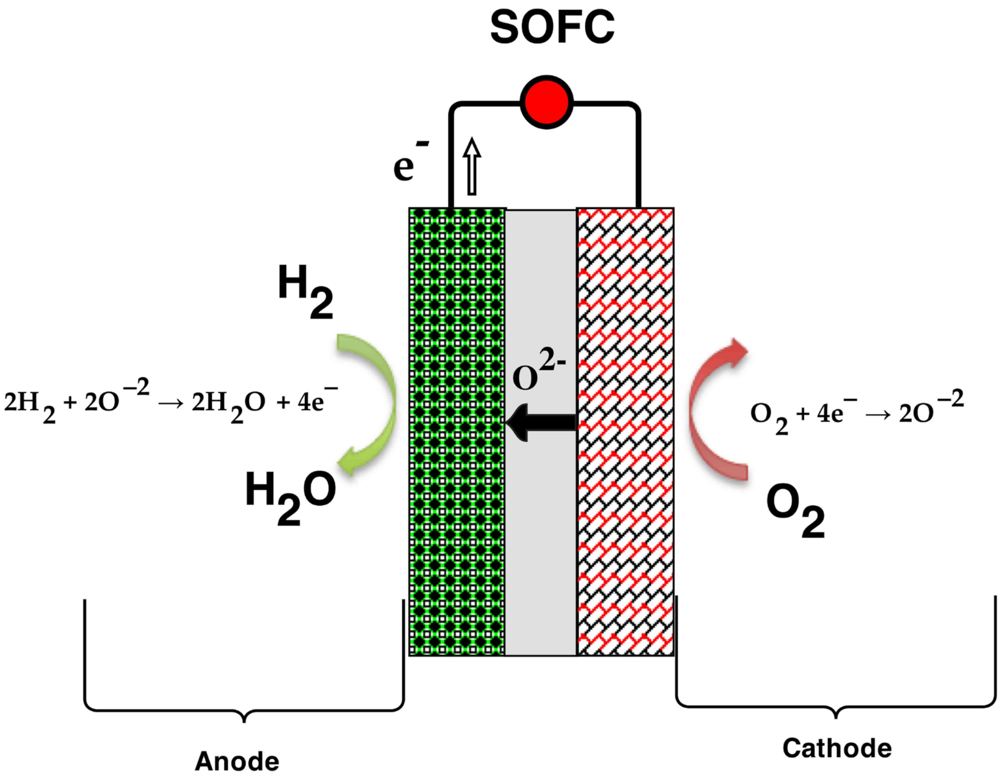

Figure 1: Schematics of a SOFC using hydrogen gas as the fuel. H_2O is produced on the Anode.

2.3 SAFCs

Solid acid fuel cells (SAFCs) are based on solid acids of selenates, phosphates, arsenates or sulphates of caesium that exhibit a super-ionic phase transition that is accompanied by a jump in proton conductivity by orders of magnitude. They can operate at temperatures of ~250 °C on either hydrogen or methanol [15-17]. The proton, H^+, is the charge carrier.

2.4 MCFCs

Molten carbonate fuel cells operate at temperatures of ~ 650 °C. In this case the carbonate anion (CO_3^{2-}) is the charge carrier. Typically $LiKCO_3$ salt in a molten state serves as the electrolyte with carbon based fuels easily being utilized. The cells are most suited for stationary applications and offer high resistance to impurities yet suffer from short life spans due to corrosion of both the anode and cathode.

Anode Reaction: $2CO_3^{2-} + 2H_2 \rightarrow 2H_2O + 2CO_2 + 4e^-$

Cathode Reaction: $2CO_2 + O_2 + 4e^- \rightarrow 2CO_3^{2-}$

Overall Cell Reaction: $2H_2 + O_2 \rightarrow 2H_2O$

2.5 PCFCs

Proton conducting fuel cells (PCFCs) are based on a ceramic electrolyte that conducts protons H^+ such as Indium-doped $BaZrO_3$ [18-20] or Yttrium-doped $BaZrO_3$ [21-25] among others. They operate in the intermediate range of 200-600 °C and can be fuelled by H_2 gas. The advantage of this setup compared to the SOFCs is that water does not dilute the fuel on the anode side as it is produced on the cathode side as shown in figure 2. Further by being capable of operating at lower temperatures, cheaper interconnects can be used and the amount of insulation required is reduced.

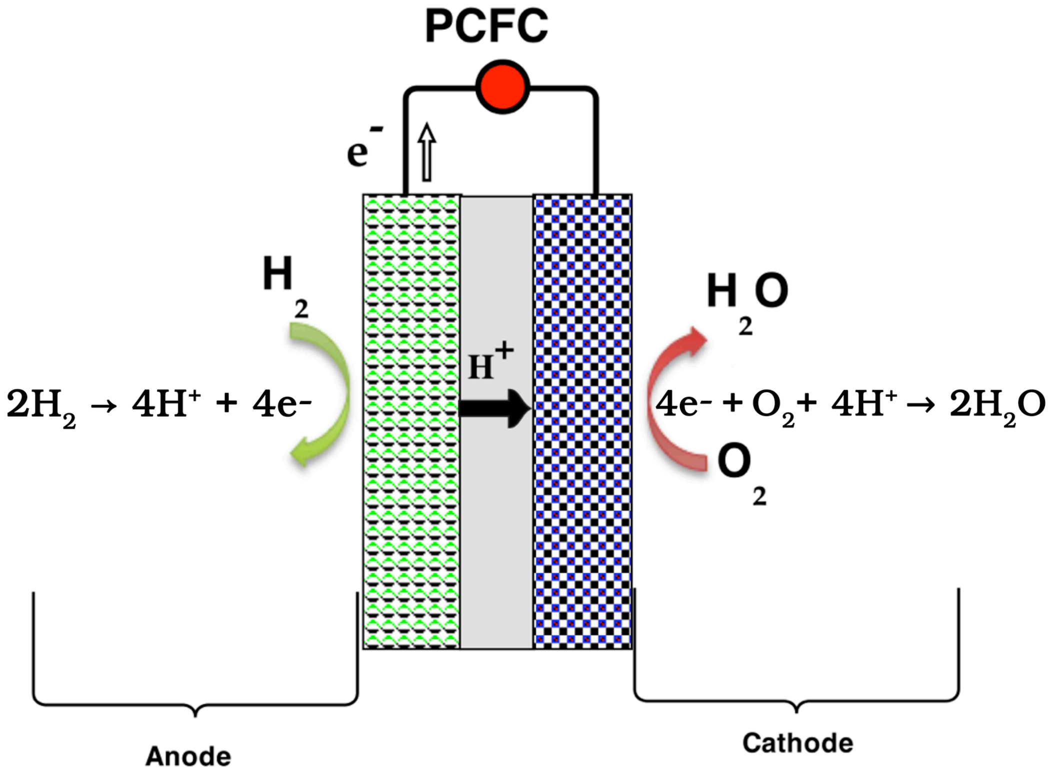

Figure 2: Schematics of a PCFC using hydrogen as a fuel and showing that H_2O is produced at the cathode.

3. Solid Electrolytes

An electrolyte is a compound that, when dissolved in a solvent, splits into positively charged cations and negatively charged anions i.e. it ionizes. Solid electrolytes, on the other hand, are materials that act as solid-state ionic conductors bringing about the movement of ions via empty crystallographic positions (vacancies) in their crystal lattice structure. Consequently the tuning of the crystal structure and vacancy formation has direct consequences on the ionic conducting properties of the material. These materials are crystalline in that they possess atomic order on the long range. However, no crystalline materials exist without defects, as no structure is perfect and deviations in the perfect arrangement will exist at all temperatures.

3.1 Types Of Defects

Commonly defects are classified using the dimensional aspect. Consequently a point defect is a 0-dimension defect and a line defect is a 1-dimensional defect etcetera.

- 0-dimensional (point defects)
    - Substitution of one atom on a site by a foreign atom of equal, lesser (acceptor doping) or greater (donor doping) charge. It is a type of extrinsic defect.
    - Interstitials, a type of intrinsic defect in which an atom sits in the space between normal crystallographic positions.
    - Interstitial foreign atoms.
    - Schottky defect [26], equal number of positively charged and negatively charged ions are absent at their lattice sites.
    - Frenkel defect, a smaller ion displaced from its lattice position into an interstitial site with the accompanying created vacancy.
- 1-dimensional (line defects)
    - Edge dislocation, an extra half-plane of atoms among full planes of atoms

  in a crystal
  - Screw dislocation
  - Row of point defects such as vacancies
- 2-dimensional (planar defects)
  - Stacking faults
  - Grain boundary
- 3-dimensional defects such as secondary phases.
- Electronic defects such as holes ($h^{\cdot}$, positively charged) and electrons.

3.2 Migration Of Defects

Migration of defects occurs when point defects move through the crystalline sample. Since a sample may poses a variety of defects, there are various diffusion mechanisms present in a sample brought about by differences in mass, charge and their electronic structure. Defect diffusion is also affected by temperature, grain boundaries, pressure and the crystal structure. A brief overview of some diffusion mechanisms is presented below.

3.2.1 Proton diffusion

Protons, H^+, being extremely small (8.768(69) fm) [27], and having a naked nucleus, tend to associate with electron clouds of other atoms such as oxygen when incorporated into the structure of a material. There are two possible mechanisms for its diffusion namely, the vehicle mechanism and the Grotthuss mechanism. In the vehicle mechanism the proton is carried on another ion that then diffuses through the structure. In the Grotthuss mechanism[28] the proton migrates via two steps, first it reorients about an oxygen atom to which it is attached and secondly jumps to the next oxygen atom breaking its original bond and forming a new bond. The accepted mechanism in protonic conducting ceramics is the Grotthuss mechanism [29, 30] as illustrated in figure 3.

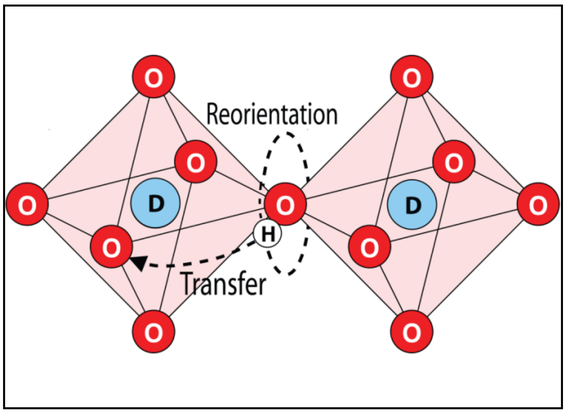

Figure 3: The Grotthuss mechanism for proton transport in acceptor-doped perovskites. Two neighbouring octahedra each made up of a dopant cation D, surrounded by six oxygen anions and sharing a corner whose oxygen has a proton attached to it. With permission from reference[31]

3.2.2 Vacancy diffusion

This takes place when an atom occupying its regular lattice site hops to a nearby vacant lattice site irrespective of its state of charge. Most important is that the atom doing the jump has a similar size as the vacancy it hops on to. This is the diffusion mode preferred in oxide ion conducting materials.

3.2.3 Interstitial diffusion

When a diffusing interstitial atom happens to be sufficiently small compared to the other atoms sitting at regular positions it can simply move from one interstitial position to another.

3.2.4 Indirect Interstitial diffusion

Occurs when an atom located at an interstitial position kicks out an atom occupying a regular lattice position and occupies it while at the same time the displaced atom moves on to occupy another interstitial site. Overall the interstitial atom has moved from one site to another.

3.3 Electrical Conductivity Of Oxides

The inverse of resistivity of an oxide is referred to as electrical conductivity (σ_i) and refers to the capability of a material to electrically conduct or transport charged species (i). A number of charged species may be conducted at any particular temperature, pressure, and reducing or oxidizing conditions. Hence in terms of current density (J_i) and the electric field strength (E), of a specie (i), the electrical conductivity (σ_i) as equation 1:

Equation 1. $\sigma_i = \frac{J_i}{E}$

Additionally the product of the charge (q), mobility (μ) and concentration (C_i) of the charged specie is also referred to as conductivity (σ_i), equation 2, which can alternatively be expressed as the diffusivity, effectively introducing the importance of temperature as per equation 3 where T is the absolute temperature and k_B is Boltzmann's constant ($8.617\,3324(78)\times10^{-5}$ eV K^{-1}, the molar gas constant divided by Avogadro's number). The temperature dependence results in Arrhenius behaviour if the charged specie's concentration C_i, is held constant, see equation 4.

Equation 2 $\sigma_i = \frac{J_i}{E} = q.\mu_{H^+}.C_{H^+}$

Equation 3 $\sigma_i = \frac{(q.D)}{(k_B.T)}$

Equation 4 $\sigma_i = A.e^{(-E_a/RT)}$

Where A is a pre-exponential term containing many factors among them the number of mobile species, charge of the species, the number of directions for the jump event, the frequency of the jumps and the volume of the system. E_a is the activation energy required to be overcome for the conduction process to occur and R is the molar gas constant.

If considering a proton conductor, given that the frequency of the jump in proton conductors concerns the O-H bond stretching vibrations, it clear that substitution for a heavier isotope in this case deuterium D^+, would result in slower vibrations of the bond and hence yield a lower jump frequency. Consequently the conductivity of the heavier deuterium isotope (atomic mass = 2.014 u) would always be discernibly lower than that of the lighter isotope, the proton (atomic mass = 1.007 u). This phenomenon is used as a dependable test to verify that indeed proton conduction is present in a sample [32]. It is referred to as the isotope effect. The units for σ_i are Siemens per centimetre (S cm^{-1}) given the centimetre scale samples used in research.

3.4 Perovskites As Proton Conductors

The perovskite structure is unique in being so versatile in the range of properties materials with the structure display. For example perovskites show magnetism [33], catalytic behaviour [34], oxide ion conduction [35] and proton conduction [25], leading to applications in areas such as gas sensors, electrolytes and thermal barrier coatings. An ideal perovskite can be described by the general formula ABO_3 that consists of corner sharing BO_6 octahedra with the A cations aligned in cubic close packed layers together with the oxygen anions as shown in figure 4. Each A-site cation has 12 nearest neighbour oxygen anions and is bigger than the B-site cation. In this thesis $A^{2+}B^{4+}O_3$ are dealt with. Stability and distortion from the cubic phase is controllable by playing around with both charge and size of the A and B cations. For a smaller than ideal A-site cation the BO_6 octahedra tilt to fill up space while for a larger than ideal A-site cation the BO_6 shrinks to compensate.

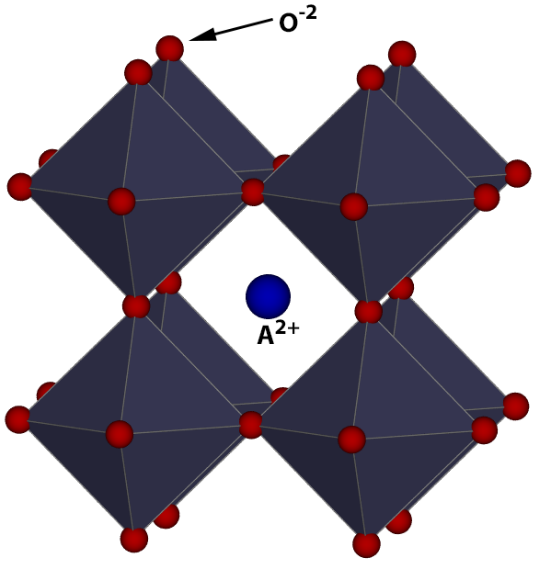

Figure 4: The structure of a cubic ABO_3 perovskite showing the location of the big A^{2+} site and the O^{2-} site. The B^{3+} site is located within the octahedra made up of six O^{2-} sites

3.4.1 Acceptor doped perovskites

Acceptor doping refers to the substitution of the tetravalent B-site cation with one of a lower valence state (e.g. M^{3+}) hence forming extrinsic defects in the form of oxygen vacancies. Typical perovskites include $BaZrO_3$, $PbZrO_3$, $BaCeO_3$ [36] and $BaSnO_3$ [37-43] among others. The doping of the ABO_3 type perovskite with a trivalent metal cation, M on the B-site, results in the formation of $x/2$ oxygen vacancies where x is the fraction of the dopant, and the resulting perovskite formula can be written as $AB_{1-x}M_xO_{3-x/2}$. In the Kröger-Vink [44, 45] notation the doping can be notated stepwise as,

Equation 5. $\mathrm{AO} + \mathrm{BO_2} \rightarrow \mathrm{A_A^{\times}} + \mathrm{B_B^{\times}} + 3\mathrm{O_O^{\times}}$ (Un-doped system)

Equation 5.1 $2\mathrm{BO}_2 + \mathrm{M}_2O_3 \rightarrow 2\mathrm{B}_\mathrm{B}^{\times} + 2\mathrm{M}_\mathrm{B}' + 5\mathrm{O}_O^{\times} + \mathrm{V}_\mathrm{O}^{\bullet\bullet}$ (doped B-site)

Where $\mathrm{B}_\mathrm{B}^\mathrm{x}$ denotes a B cation sitting on a regular B-site and a neutral charge (×), $\mathrm{O}_\mathrm{O}^\mathrm{x}$ denotes an oxygen anion sitting on a regular oxygen site and $\mathrm{V}_\mathrm{O}^{\bullet\bullet}$ denotes an oxygen site with an effective charge of +2 (••). M_B' denotes the dopant trivalent cation sitting on a regular B-site resulting in an effective negative charge. The Kroger-Vink notation for negatively charged electrons is e' and $\mathrm{h}^\bullet$ for positively charged holes. Generally small trivalent cations such as Yb^{3+} (0.86 Å) [26, 46, 47] substitute for the B-site while larger cations such as La^{3+} (1.03 Å) substitute on the A-site [26, 42] .

When the acceptor doped perovskites are exposed to a humid atmosphere the oxygen vacancies get substituted for by hydroxyl groups of which the oxygen sits on the vacant oxygen site and the remaining proton (H^+) occupies an interstitial site. This can be represented as,

Equation 6. $\mathrm{H_2O_{(g)}} + \mathrm{V}_\mathrm{O}^{\bullet\bullet} + \mathrm{O}_\mathrm{O}^\mathrm{x} = 2[\mathrm{OH}]_\mathrm{O}^{\bullet}$

Under reducing conditions *i.e.* low oxygen partial pressures, the sample may lose oxygen and hence electrons form as described below,

Equation 7. $\mathrm{O}_\mathrm{O}^\mathrm{x} = ½\mathrm{O}_{2(\mathrm{g})} + \mathrm{V}_\mathrm{O}^{\bullet\bullet} + 2\mathrm{e}'$

Alternatively, in oxidizing conditions *i.e.* high oxygen partial pressures, the following can occur resulting in the formation of electronic holes ($\mathrm{h}^\bullet$),

Equation 8. $½\mathrm{O}_{2\,(\mathrm{g})} + \mathrm{V}_\mathrm{O}^{\bullet\bullet} = \mathrm{O}_\mathrm{O}^\mathrm{x} + 2\mathrm{h}^\bullet$

3.4.2 Current Status of Proton Conductors

In the early 1980's Iwahara and co-workers [48] demonstrated proton conduction in doped SrCeO3 which marked the beginning of intense scientific interest into proton conduction in perovskites and related phases such as the brownmillerites. To date $BaCeO_3$ doped with acceptor dopants on the B-site has demonstrated the highest proton conduction so far with $BaCe_{0.9}Y_{0.1}O_{3-\delta}$ being at the top [49, 50]. However it suffers from its ease of reaction with CO_2 and steam [51, 52] due to its high basicity. Alternatively $CaZrO_3$ is less basic and hence more chemically and also mechanically stable than $BaCeO_3$ [49]. It possesses a much lower protonic conduction but is used industrially as a hydrogen sensor in the manufacture of aluminium alloys [53]. The acceptor doped perovskite $BaZrO_3$ has come to the forefront of proton conduction research due to its good chemical stability albeit with slightly lower proton conductivity [54].

$BaZr_{0.8}Y_{0.2}O_{3-\delta}$ [25] is currently regarded as the leading option and is, an almost pure proton conductor at temperatures below 650 °C. The compound has two main challenges, the high temperatures required in achieving high densification and secondly the poor grain boundary conductivity [55, 56]. The former presents a manufacturing challenge in the production of fuel cell stacks, as the electrodes of a fuel cell are required to possess a certain degree of porosity and yet high temperatures decrease their porosity. The poor grain boundary conductivity lowers the total conductivity of the ceramic samples [56].

These challenges can be overcome by reducing the total number of grain boundaries through the use of sintering aids such as ZnO [57] and NiO [58, 59] or through the use of nano-scale starting materials for fabrication. The use of epitaxially grown thin films has further improved the conductivity of $BaZr_{0.8}Y_{0.2}O_3$ to the extent that part of "Norby's gap" [60], figure 6, has been partially filled, figure 5 [61].In figure 5 converting the required area specific resistance (ASR) of 0.15 Ω cm^2 to the log scale of figure 6, we get a y scale value of -0.175 S cm^{-1} for $BaZr_{0.8}Y_{0.2}O_{3-\delta}$ above 425 °C at which point the conductivity is above 1×10^{-2} S cm^{-1}. Alternative oxide systems showing proton conductivity include Sr/Ca-doped $LaNbO_4$ [62] with a total conductivity of 2×10^{-4} S cm^{-1} in wet hydrogen at 600 °C, $Ba_3Ca_{1.18}Nb_{1.82}O_{9-\delta}$ [63] with 1.8×10^{-4}S cm^{-1} at 700 °C.

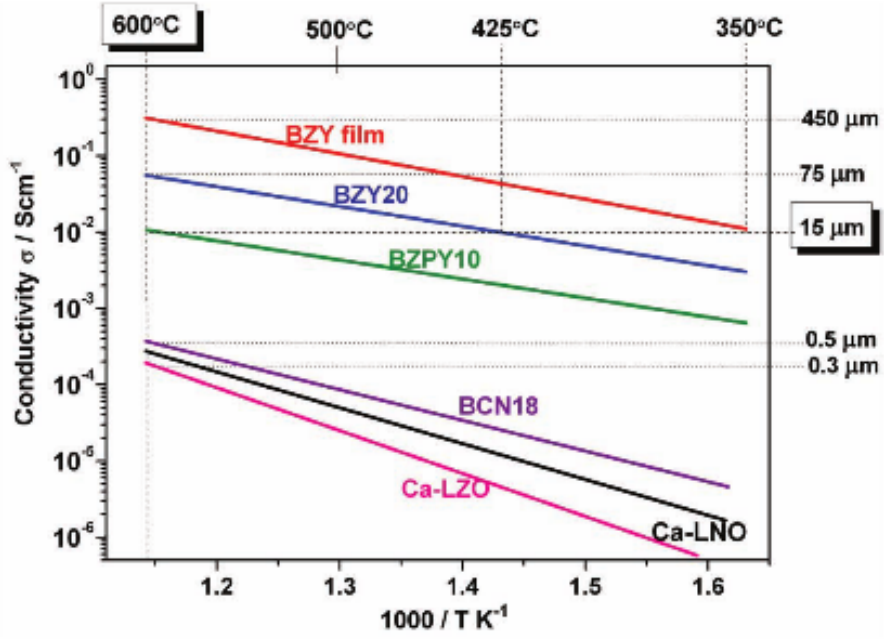

Figure 5 The total conductivity values for select proton conductors as of 2012, $BaZr_{0.8}Y_{0.2}O_{3-\delta}$ (BZY20) film and pellet, $BaZr_{0.7}Pr_{0.1}Y_{0.2}O_{3-\delta}$ (BZPY10), $Ba_3Ca_{1.18}Nb_{1.82}O_{9-\delta}$ (BCN18), $Ca_{0.01}La_{0.99}NbO_4$ (Ca-LNO), $La_{1.95}Ca_{0.05}Zr_2O_7$ (Ca-LZO). The maximum electrolyte thickness for a given electrolyte to achieve the target value for the area specific resistance (ASR) of 0.15 Ω cm^2 is shown on the right axis. The figure also allows estimating the operating temperature for a given electrolyte keeping fixed the electrolyte thickness at 15 µm for an ASR of 0.15 Ωcm^2. Adopted with permission from reference [61]

Our in-house research has so far focused on acceptor doped $BaZrO_3$ compositions with In^{3+} [18] as the most common dopant. Other dopants investigated include Yb^{3+} [64] Sc^{3+} [65]and Ga^{3+} [66].The location of the proton site in the 50%In:$BaZrO_3$ has been described [67]. The effects of wet chemical preparation versus solid state synthesis of 50%In:$BaZrO_3$ has been investigated and their effect on conductivity demonstrated [68].

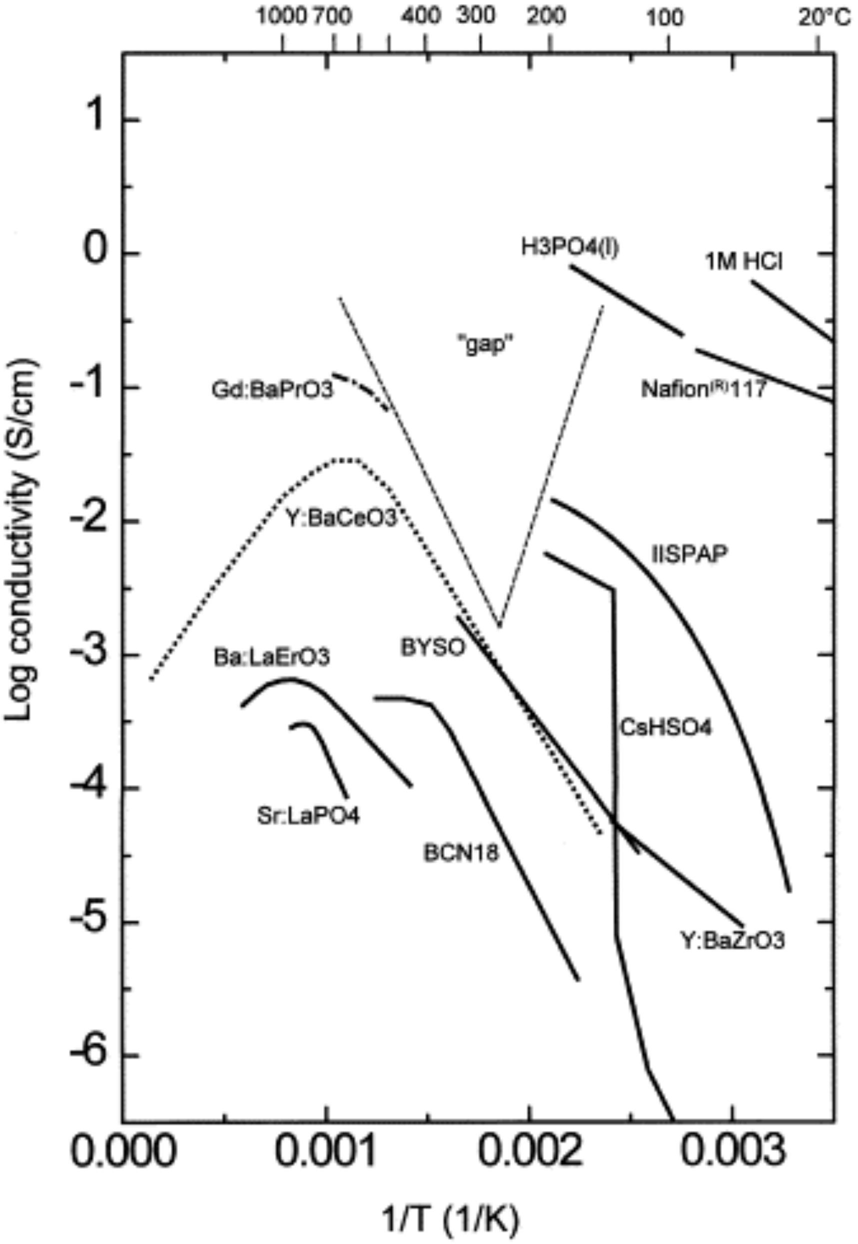

Figure 6 An overview of selected literature data as of 1999 for proton conductivity as a function of inverse temperature. IISPAP, imidazole-intercalated sulfonated polyaromatic polymer; BYSO, $Ba_2YSnO_{5.5}$. The curve for Y:$BaCeO_3$ is a calculated estimate. The interpretation of the conductivity of Gd:$BaPrO_3$ has been shown to be a hole conductor. Graph adopted with permission from reference [60]

The works herein attempt to increase both bulk and grain boundary conductivity through the use of spark plasma sintering and co-doping of In:$BaZrO_3$. A further step is taken to investigate the effect of tuning the conductivity in $Ba_3In_2ZrO_8$ ($BaIn_{0.66}Zr_{0.33}O_{2.67}$) with GaY or GdY combinations. An alternate system, Sc:$BaSnO_3$ is investigated to elucidate its structure and conductivity.

3.5 Pyrochlores And Fluorites As Oxide Ion Conductors.

The fluorite structure, is named after the mineral CaF_2, and can be thought of as having a general formula of BO_2 ($B^{4+}O_2^{2-}$) and fluorites belongs to the $Fm\bar{3}m$ space group, figure 7.The cations occupy the corners and centres of the cubes faces while the 4 anion atoms form a smaller cube inside.

Pyrochlores, of the formula $A_2B_2O_7$, are related to the mineral pyrochlore, (NaCa)(NbTa)O_6F/OH from which they are named. Two families exist with different charge combination on the A-site and B-site, (3+, 4+) or (2+, 5+) and consequently their formulae are, $A_2^{3+}B_2^{4+}O_7$ and $A_2^{2+}B_2^{5+}O_7$ respectively. Only the former is dealt with in this thesis. Typically a completely cubic pyrochlore belongs to the $Fd\bar{3}m$ space group. By fixing the unit cell's origin at its B-site the structure can be described as having four distinct atomic positions, A at 16*d*, B at 16*c*, O at 48*f* and O* at 8*b*. Hence its general formula is more appropriately written as $A_2B_2O_6O^*$ indicating the two distinct oxygen sites.

Pyrochlores, figure 8, are related to fluorites, figure 7. An $\frac{1}{8}$ of a pyrochlore's unit cell can be visualized as a full fluorite unit cell with an unoccupied 8*a* site and half of the B^{4+}cations replaced with A^{3+}cations to achieve charge neutrality as shown in figure 8. The pyrochlore structure has significant relaxation, from the ideal positions (figure 7) of surrounding 48*f* anions towards the unoccupied 8*a* site, figure 9.

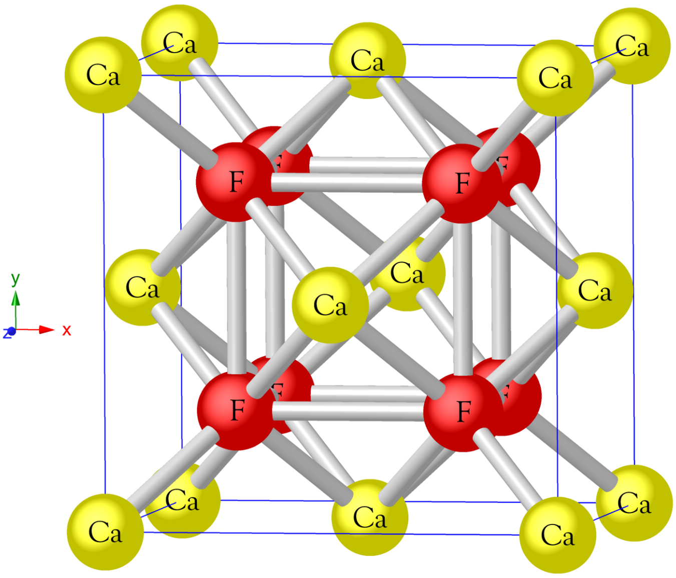

Figure 7: The structure of a fluorite (CaF_2) showing the fully occupied anion sites and that there is no relaxation of the anions (right).

Whenever the ionic sizes of the A and B cations become similar in the $A_2B_2O_7$ compounds there is a likelihood that an order-disorder transition into an oxygen deficient, disordered fluorite structure, will occur. In which case the A and B site cations randomly occupy each other's positions [69]. Further disorder can occur in the anion sub-lattice resulting in the normally vacant 8*a* position being partially filled while the vacancies shift to the 8*b* or 48*f* sites that are normally filled. The pyrochlore-fluorite transition can also occur as a function of temperature in certain compositions close to the pyrochlore-fluorite phase boundary [69]. A pyrochlore stability region exists for ratios of the A^{3+}:B^{4+} ionic radii between 1.46-1.78 Å where the cubic pyrochlore structure is exhibited [69, 70]. Examples of pyrochlores include $Y_2Ti_2O_7$ [71], $Gd_2Zr_2O_7$ [72] and $Sm_2Ti_2O_7$ [73].

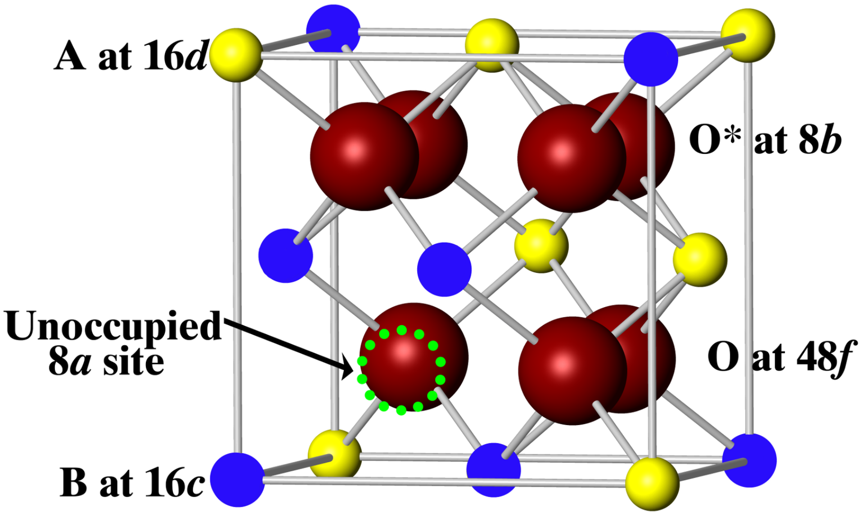

Figure 8: The ideal pyrochlore structure represented by a ⅛ cuboid of the unit cell in the style of a fluorite unit cell showing the vacant anion 8*a* site indicated by the dotted circle. The six 48*f* sites are occupied by oxygen anions coordinated to two A-site and two B-site cations and the 8*b* site is coordinated to four A-site cations respectively in the above representation.

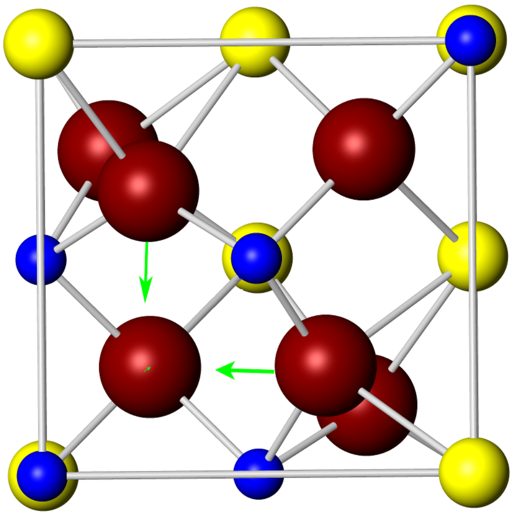

Figure 9: A real pyrochlore structure ($Y_2Ti_2O_7$) represented by a ⅛ cuboid of the unit cell in the style of a fluorite unit cell showing the relative relaxation of the neighbouring atoms towards the vacant anion 8*a* site indicated by the arrows.

3.5.1 Current status of oxide ion conductors

ZrO_2 that has been acceptor doped and stabilized to the cubic fluorite structure at lower temperatures, T<1000 C, possess significant amount of vacancies necessary to facilitate oxide ion conduction via vacancy hopping. Divalent cations, M, or rare earth trivalent cations, R, can substitute the cation site on the host lattice to generate vacancies as denoted in the Kroger-Vink notation below,

Equation 9. $\mathrm{MO} + \mathrm{Zr}_{Zr}^{\times} = \mathrm{M}_{\mathrm{Zr}}'' + \mathrm{ZrO_2} + \mathrm{V}_{\mathrm{O}}^{\bullet\bullet}$

Equation 10 $\mathrm{R_2O_3} + 2\mathrm{Zr}_{Zr}^{\times} + \mathrm{O}_{O}^{\times} = 2\mathrm{R}_{\mathrm{Zr}}' + 2\mathrm{ZrO_2} + \mathrm{V}_{\mathrm{O}}^{\bullet\bullet}$

Typical dopants include Ca^{2+}, Sc^{3+} and Y^{3+} with the resultant ceramics being named as calcia-stabilized zirconia (CSZ), scandia-stabilized zirconia (ScSZ) and yttria-stabilized zirconia (YSZ) respectively [74]. YSZ has high oxide ion conductivity above 700 °C [75] and is currently the most widely used electrolyte material in SOFCs.

Doped CeO_2 have also been known to be good oxide ion conductors [76]. Of this type samarium-doped ceria (SDC) and gadolinia-doped ceria (GDC or CGO) possess significantly higher conductivity than YSZ between 500-700 °C. Their only limitation is in low oxygen partial pressures at temperatures >600 °C where a non-negligible electronic conduction is observed as the cerium host cation is reduced to a trivalent state [77]. There exists an optimum doping level from which conductivity is lowered with increasing dopant concentration [78].

The anion deficient delta phase of Bismuth oxide, δ-Bi_2O_3, has the highest known oxide ion conduction at 2.3 S cm^{-1}at 880 °C [79]. Unfortunately it is apt to corrode almost all the other cell components at the operating temperatures hence limiting its applications in fuel cells. Substitution of part of the bismuth with yttrium gadolinium niobium or tantalum among other cations stabilizes the delta phase to lower temperature but lowers the conductivity [80].

Most of these compounds have a fluorite or fluorite related structure. Therefore it's increasingly important to study the crystal structure and its relationship to the behaviour of conductivity to understand exactly how the cation, anion and vacancy ordering affect the oxide ion conductivity. Ideally a system with a high oxide ion vacancy concentration should result in good oxygen ion conductivity. But what happens if for example the oxygen ion vacancies order in a specific manner in the crystal structure? What if the cations order? In this thesis the pyrochlore structured $Y_2Ti_2O_7$ transition to the disordered fluorite structured $Zr_2Y_2O_7$, of the ZrO_2-TiO_2-Y_2O_3 ternary system is studied with reference to its effect on the electrical conductivity for a series of compositions, $Y_2(Ti_{1-x}Zr_x)O_7$ with $x = 0.00, 0.15, 0.30, 0.40, 0.50, 0.65, 0.80$, and 1.00. The conduction mechanism in these types of oxides is based on the jumping of vacancies through the structure.

3.6 Mixed Ionic-Electronic Conductors (MIEC) For Proton Conducting Fuel Cells

These are materials possessing both protonic and electronic conduction. They are suitable for electrode applications. However to allow for the gas to solid interface reactions they need to possess a large surface area and extend their reaction area through the entirety of their bulk in addition to their interface with the electrolyte. This is very important on the cathode side. Where oxygen adsorbs, dissociates, is reduced and diffuses on the surface and in the bulk. Proton migration, water formation and evaporation also occur on the cathode side. Therefore simultaneous migration of electrons protons and oxygen has to occur in the cathode materials.

$BaCe_{0.8-x}Pr_xGd_{0.2}O_{3-\delta}$ [81] ($\sigma_T(the\ total\ conductivity)$= 0.75 S cm^{-1} in air at 800 °C) and Yb:$BaCeO_3$ [82] (above 600 °C, σ_T= 2.3 × 10^{-2} S cm^{-1} in wet oxygen at 800 °C) are some of the materials that have recently been reported to possess mixed ionic-electronic conduction. Both of these compounds react with CO_2 and water vapour [52, 54, 83]. $BaZr_{0.8-x}Pr_xY_{0.2}O_{3-\delta}$ (x=0.2, 0.3) has been reported as having good chemical stability but however has insufficient mixed conductivity for application as a cathode [84]. The high surface areas required can be met by wet chemical synthesis followed by relatively low temperature (~1000 °C) co-firing of the fuel cell. In this thesis we report on the accidental discovery of MIEC in a complex, disordered perovskite, $Ba_3In_{1.4}Y_{0.3}Ga_{0.3}ZrO_8$.

3.7 Materials Requirement For The Electrolyte

As a requirement for a good electrolyte the material should be impermeable to gas, be highly dense, block electron conduction and possess ionic conduction of the order $\sigma = 10^{-2}\ \mathrm{S\,cm^{-1}}$ for practical use. One of the challenges is that some materials are not easily sinterable and therefore possess a lot of grain boundaries, which reduces the total conductivity. To overcome this, sintering additives [21], wet-chemical [19] /SOL [85], and epitaxially grown thin films are used to improve densification at lower temperatures hence reducing the number of grain boundaries present. Further SPS [86] is used to reduce the resistance at the grain boundaries towards defect transport. These strategies often result in higher conductivity and improved overall fuel cell performance.

4. Experimental techniques

4.1 Sample Preparation

4.1.1 Solid State Synthesis

In this work solid state synthesis (SSS) describes the synthesis of materials in which stoichiometric quantities of the metal carbonates and oxides, which have been heated to remove moisture before weighing, are mixed in an agate mortar and hand milled with a pestle in the presence of ethanol (99.5%). The dried powder is then

1. Calcined at 1000 °C for a given number hours to decompose the carbonates.
2. Pressed into pellets and heated to a higher temperature for a given time span.
3. The pellet is crushed and milled, the resulting powder is checked for purity using X-ray powder diffraction and, if found not pure, step 2 and 3 are repeated until the sample is found to be pure.

Occasionally ball milling with a planetary ball mill is employed in the intermediate stages between the heating steps especially when large sample quantities (>5g) are required in a series of compounds. The milling balls and the milling house can be made of alumina, zirconia or steel. A typical milling run has the following parameters: 500 rpm, 20 minutes of milling, 5 minutes of cooling and 40 repetitions.

Solid state reactive sintering, SSRS, is a modified solid-state synthesis route whereby the complete reaction and the sintering to higher densities of a sample occur in one single step. Hence only steps 1 and an extended step 2 are performed to yield a high-density sample.

4.1.2 Spark plasma sintering (SPS)

In this densification technique the sample is made dense by holding it under pressure in a graphite die under vacuum conditions while passing a pulsed DC current through the graphite and sample to provide heating. Pure sample powders are ball milled into fine powders and put in a graphite pressure die and then mounted onto a die stage inside the SPS equipment, in this case a “Dr. Sinter 2050” (Syntex Inc., Japan) SPS setup. The die chamber is evacuated to 6 Pa and a pulsed DC current is applied through the die. This rapidly heats the sample under pressure (100 °C/min) to a desired final sintering temperature *e.g.* 1250 °C. The sample is held at that temperature for a period of time, say 5 min at 100 MPa then cooled after switching off the current and releasing the pressure. The sample is cooled down rapidly to room temperature. The SPS sample is then polished and oxidized at higher temperature for some time to remove traces of carbon (from the die) on the surface. The samples normally have a density of between 90-99% of the theoretical value.

4.1.3 Hydration.

The hydration is carried out at 300 °C under N_2 gas flow saturated with water vapour at 76.2 °C (~0.42 atm, $p(H_2O)$) for several days for powdered and pellet forms of the materials. Pellet samples for *in-situ* neutron diffraction combined with electrochemical impedance spectroscopy are deuterated hydrothermally by inserting them in a Teflon lined autoclave with a precise amount of D_2O equivalent to the amount of theoretical oxygen vacancies present in the sample at 210 °C for 12 hours. This can also be performed on powdered samples.

4.1.4 Pellets for conductivity.

Sintered pellets for conductivity are first polished preferably to a mirror like finish then painted with platinum ink dried at 150 °C and the organics burnt off at about 1000 °C using a very slow heating rate.

4.2 Characterization Techniques.

4.2.1 Powder Diffraction.

The primary method of characterizing the samples purity, crystal structure and reaction progress in this study was X-ray powder diffraction technique (XRPD). When a crystalline sample is irradiated with beams of X-ray or Neutron radiation of a wavelength comparable to its atomic spacing's, constructive and destructive interference of the elastically scattered beams will occur between the lattice planes in the crystal, resulting in a diffraction pattern. This pattern presents a detailed picture of the crystal structure describing it in terms of the symmetry of the unit cell and its dimensions, fractional coordinates of the atoms forming the lattice. For a pure material, all its peaks in the diffractogram can be indexed and assigned to a specific unit cell. Hence this technique is able to "fingerprint" material's since the materials X-ray pattern is dependent on the atomic number, position of the atoms, and the type of unit cell as well as its size which yield specific peaks, peak positions and relative intensities unique to a material. Therefore despite two or more materials having the same space group, their diffractograms will be essentially unique.

Crystalline materials are characterized by the orderly periodic arrangement of atoms and possess reciprocal lattice points (visible from single crystal diffraction data) described by integer values *h, k, l* known as Miller indices, in which case the distance between two of these planes is denoted d_{hkl}. In reciprocal space however the distance between reciprocal space planes is ascribed $\frac{1}{d_{hkl}}$. The reciprocal space is a Fourier transform of the direct space in which the unit cell exists. Given a monochromatic X-ray beam and a set of parallel planes in the crystal, constructive interference will occur only if the Bragg conditions are fulfilled. These conditions are: the path length difference between two waves constructively interfering is a multiple integer (n) of the wavelength and the wavelength (λ) is comparable to inter-atomic distances (inter-lattice distances). The constructive interference will result in peaks appearing in the collected diffraction pattern plotted as the intensity as a function of 2θ. This is articulated in the Bragg equation below.

Equation 11 $$2d_{hkl}\sin\theta = n.\lambda$$

For a material like $BaZr_{0.5}In_{0.5}O_{3-\delta}$ that has a cubic unit cell, then the cell parameter "a" can be calculated as below,

Equation 12 $$a^2 = d^2(h^2 + k^2 + l^2)$$

Where *h,k,l* are the Miller indices , *d* is the inter-planar spacing (figure 10) . The Bragg equation is illustrated below whereby a set of lattice points (dots) in a line represent planes of atoms in a sample, while the two parallel X-ray beams are represented by wavy lines, *d* is the inter-planar distance and θ is the incident angle to the plane. The path difference between the beams, CBD *i.e.* CB+BD, is hence equivalent to $2d\sin\theta$. To pinpoint the expected peak positions the two equations (11 and 12) can be combined for a cubic system as:

Equation 13 $$\sin^2\theta = (h^2 + k^2 + l^2)\left(\frac{\lambda}{2a}\right)^2$$

The detector samples the diffracted beams intensities over a 2 θ angular range, which itself is the angle between the diffracted beam and the incident beam. The powder diffraction analysis utilizes the diffraction peak intensity, profile, and 2 θ position to reveal the crystal structure of the samples being studied. The relative concentration of different phases in the sample, the atomic arrangement in the different phases and the identity of those phases can hence be obtained.

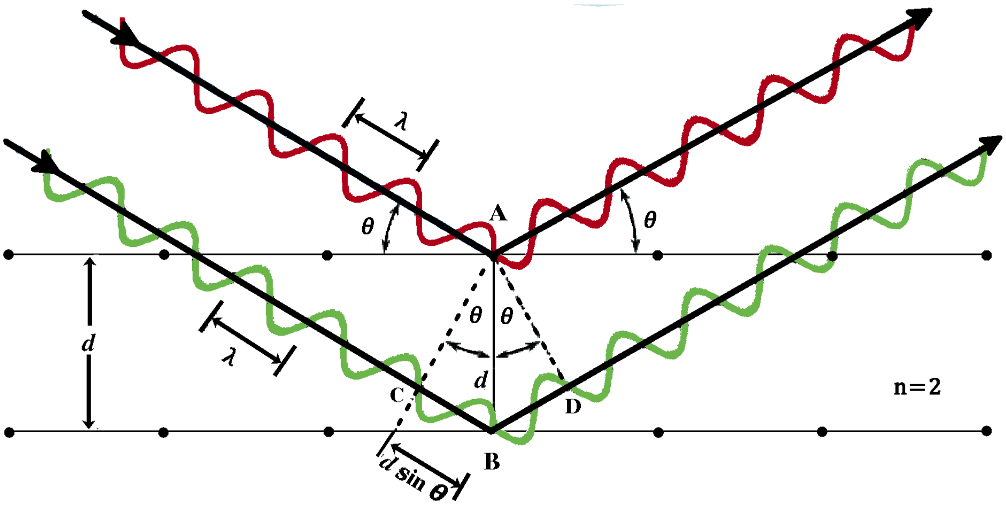

Figure 10: An illustration of the Braggs law showing that the path length difference travelled by the second X-ray beam (green), CBD can be calculated using $2d\sin\theta$ where d is the interplanar distance, θ is the incident angle.

The X-ray instrument used in this project was the Bruker D8 Advance™ diffractometer with a monochromatic Cu Kα_1 radiation with a wavelength of 1.54056 Å. The ICDD (International Centre for Diffraction Data) database was used to identify the phases in the sample.

Neutron powder diffraction (NPD) was performed at the POLARIS [87] beam line at the ISIS neutron facility, a short pulse spallation source located in the U.K.. Neutrons for diffraction studies are generated from nuclear reactors or spallation sources. In a reactor source the neutrons produced as a result of fission processes while in a spallation source targeting high-energy protons on a suitable metal target produces the neutrons. In the former source the neutrons are produced continuously while pulses of neutrons are produced from spallation sources.

Among the advantages of using NPD is that diffraction from the nuclei by neutrons has no form factor hence the peak intensity in the diffractogram does not decay with increasing 2θ values unlike in X-ray powder diffraction (XRPD). Further in NPD the scattering power of the atoms is not dependent on the number of electrons hence the positions of light atoms such as hydrogen (by substitution with its heavier isotope D) and oxygen can be identified in the presence of heavier atoms unlike in XRPD. A good application of this ability is the determination of the hydrogen positions in metallic hydrides such as europium hydride [88], a hydrogen storage candidate. Additionally the precise atomic positions are best-refined using neutron data. Oxide based superconductors require the precise location of the atoms to be determined and also the occupancy of oxygen sites to be finely refined so as to elucidate the source of superconductivity [89, 90].

The energy dispersive principle of neutron diffraction, commonly known as time of flight (TOF), is applied in pulsed neutron sources, which deliver white band neutrons (neutrons with varying speeds) on to the sample. Given a neutron travel path, the fast (shorter λ) neutrons would separate from the slow (longer λ) ones in the incident beam. All of these wavelengths (λ's) hit the sample can, made of neutron transparent material, e.g. vanadium, before being diffracted by the contained sample onto the detectors.

The scattered beams' λ is obtained by measuring the total time of flight (*t*) from the source to the sample and then to the detector given that the total flight path length (*L*) is available. Hence, *t* can be related to λ via the following equation [91],

Equation 14 $$t_{\mu sec} = 252.78 * L(m) * \lambda(\text{Å})$$

Therefore, for a wavelength (λ) of 3 Å and a path length (L) of 12 meters the TOF would be 9.10 ms. In practice it is important to achieve good resolution of the Bragg peaks by having a long flight path. This introduces a frame overlap problem that occurs due to faster neutrons overtaking slower neutrons to the detectors hence contaminating the collected data. The set of neutron λ's free of overlapping (Δλ) are obtained by considering that [91]:

Equation 15 $$t_{max} - t_{min} = \Delta t = \frac{1}{\nu}$$

Where ν is the pulse frequency of the source and hence Δλ is

Equation 16 $$\Delta\lambda(\text{Å}) = \frac{3956}{L(m) \times \nu\ (Hz)}$$

The frame overlap can be removed by inserting waveband choppers between the source and the sample to exclude a number of incident beam pulses so that instead of collecting the data in a number of wavelength sections, each Δλ in value, the entire diffraction pattern can be collected at one particular setting (a specific pulse of each cycle, ν).

For the POLARIS [87] powder diffractometer at the ISIS facility near Oxford, UK, the sample position is 12 m from the source hence the available maximum wavelength is 6.59 Å, using equation 16 (above). There are three sets of detector banks, the low angle, the 90° and the backscattering banks each covering 14°-27°, 86°-94° and 130°-155° 2 θ range respectively.

4.2.1.1 Rietveld analysis

The Rietveld method [92, 93] is a least squares refinement method that minimizes the difference between a diffraction pattern calculated from a crystallographic model and experimentally observed data. By altering different parameters such as; *zero point (detector), lattice parameters, background noise, temperature factors and atomic coordinates of the atoms,* the experimentally observed Bragg reflections' width, height and positions can be modelled. However, it is important to remember that convergence of the least-squares calculation between the pattern based on the model and experimental pattern provides no guarantee that the model is physically meaningful as the convergence of least-square calculation may occur due to false minima. Therefore, a good chemical knowledge is essential when undertaking a refinement.

An important aspect with the Rietveld method is that the user is in control of the information given through the refinement and can hence be able to re-modify the parameters as needed. This can be done by, for example, comparing the bond lengths from the Rietveld refinement with known bond lengths from literature or bond valence sum (BVS) calculations, hence avoiding unreasonable bond lengths in the refinement.

This data is then fitted into the Rietveld Analysis software such as GSAS [94] where the theoretical model is refined by altering different factors with a visual inspection of the graphical output. Typically the process involves;

- Data collection of the diffracted intensities in very small 2 θ step sizes dwelling for as long as necessary per step, and collecting data over a wide 2-theta range.
- Generating a crystal structure model either from scratch or from a database containing compounds with similar x-ray patterns.
- Modifying the peak profile parameters and background to fit the observed intensity properly.
- Least square refinements of the atomic positions, site occupancies, thermal parameters and the unit cell parameters.

4.2.2 Thermogravimetric analysis (TGA)

TGA is an experimental method in which the mass change of a sample is measured as a function of temperature or time. The mass change indicates whether the sample undergoes decomposition or absorption/desorption when heated, cooled or kept at isothermal conditions, under controlled atmospheres. In the case of decomposition it's also possible to calculate which types of molecules are lost in the process given a bit of chemical knowledge of the sample. The mass change is this case an inherent property of the material and can be quantitatively linked to physical or chemical processes occurring in the sample.

In the case of proton conductors, during the hydration process, protons are incorporated into the structure of the material, which results in an increase in mass of the sample. Similarly, for pre-hydrated samples a mass loss is observed upon heating under a dry inert atmosphere. By following the mass change of the samples quantitatively, it is possible to determine the amount of proton defects formed during the hydration process.

The instrument used for the TGA investigations was a NETZSCH STA 409 PC (Figure 11) with alumina crucibles and nitrogen gas as the supporting gas. The empty reference container and empty sample container are first run empty to create a background correction file before the sample is introduced and an identical thermal procedure repeated. A correction scan is always run before performing a new series of investigations.

Before every run the furnace outlet top valve is shut, then the vacuum pump is turned on and the chamber evacuated and refilled twice with an inert gas using the back valve for evacuation and the side valve for refilling with inert gas e.g. N_2 or Ar (to at least 1mbar). After the second refill, the vacuum and refill valves are shut and the pump is turned off. Before a run the initial gas flow conditions are turned on and the top valve outlet is opened. In general, 15 minutes time is elapsed before the measurement is started in order to ensure the gas flow has equilibrated with the set flow rate.

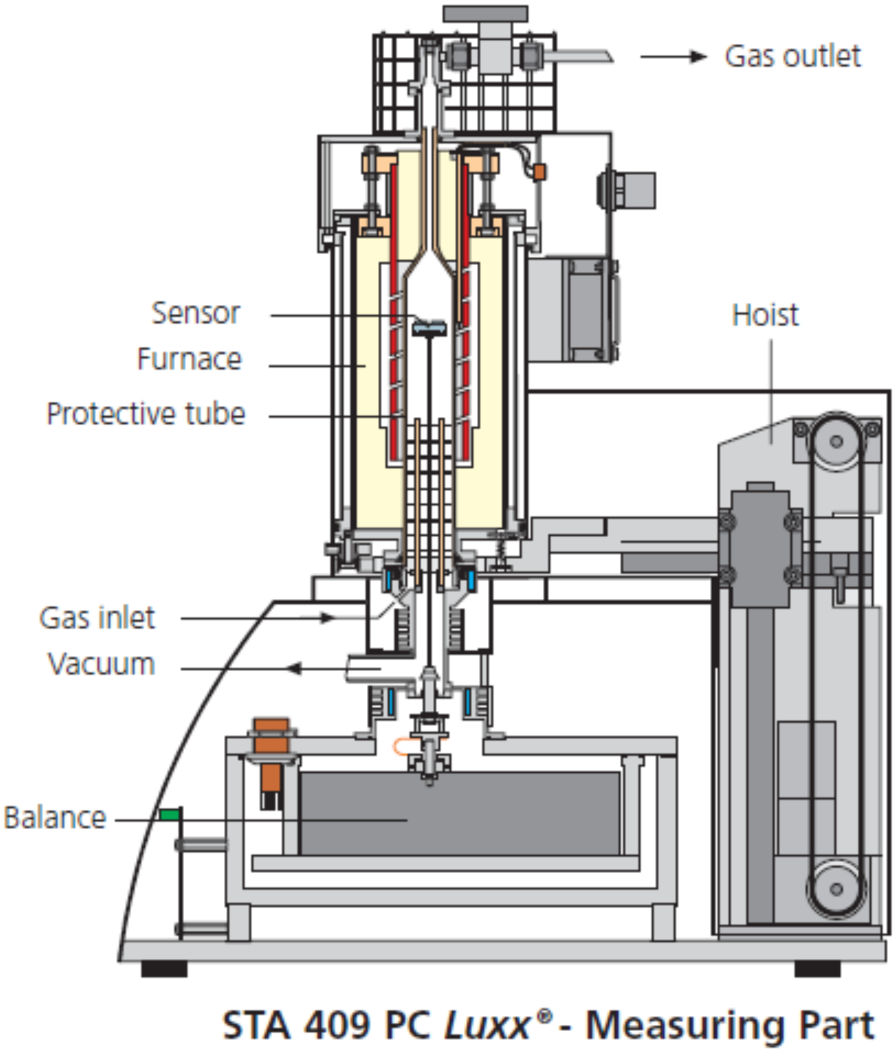

Figure 11: The schematics of a NETZSCH STA 409 PC instrument used for the TGA measurements.

4.2.3 Electrochemical impedance spectroscopy (EIS)

The method measures the electrical impedance that is frequency dependent only. In most cases a ceramic materials electrical properties are composed of various processes such as diffusion of various charge carriers and components such as grains and grain boundaries. When investigating a material, special interest is paid to separate the contributions from the grain bulk, grain boundary, electrode processes and diffusion to the electric properties of the material. Ionic conduction, defects and electric conduction can be characterized as well as ferroelectric and dielectric properties of a material.

The method samples impedance for a given range of requested frequencies at a predetermined AC voltage thereby determining the frequency responses of the sample to the applied voltage. The electrode, bulk and grain boundaries have their conductivities expressed at different frequencies and hence their semicircles (time constants) can often be resolved. Typically a complex plane plot where the imaginary impedance (Z”) is plotted against the real impedance (Z’) is used to present the results of an experiment. The data is composed of semicircles, each of which can be ascribed to the circuit elements the resistor (R) and a constant phase element (CPE), an imperfect capacitor, in parallel. For an ideal polycrystalline material, the bulk behaviour (B) is found at the high frequency region (to the left of a complex plane plot), the grain boundary (GB) in the middle frequencies and the electrode behaviour (E) in the low frequency region (to the right) as shown in the figure 12. This is due to the fact that grain boundaries generally have resistances higher than those of the grain bulk hence it is advantageous to minimize the amount of grain boundaries by having larger grains in the sample. However the contributions of the bulk and grain boundaries often overlap and then it becomes difficult to separate their semicircles.

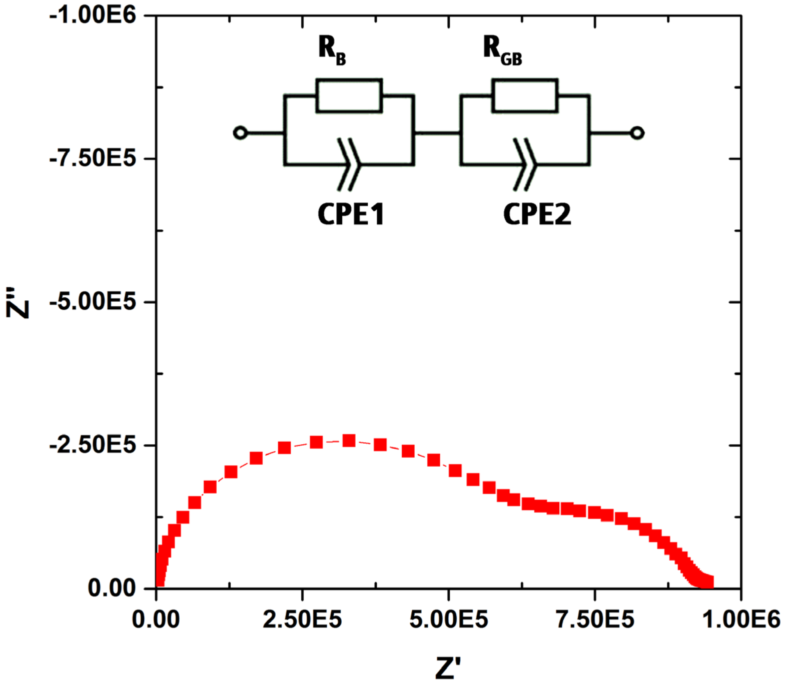

Figure 12: A typical impedance plot in the complex plane showing two semi-circles in the frequency range scan of interest and a small electrode contribution at the of the second semi circle to the right. From the left, each semi-circle represents, as modelled in the circuit above, the grain bulk (R_BQ_1) and the grain boundary ($R_{GB}Q_2$) .R denotes a resistor and Q a constant phase element.

The resistances of each of the components in a material are indicated by the distance across the semicircle along Z'. In practice the results are fitted with circuit models from which the resistances (R (Ω)) are obtained. Impedance accounts for capacitance and inductance effects, which vary with the frequency (*f*) of the electric current through the sample. Impedance is only equivalent to resistance if the circuit lacks any capacitors or inductors. Impedance (Z) is made up of two parts, the resistance R (independent of *f*) and the reactance X (dependent on *f* due to capacitance and inductance).

A phase shift between current and voltage is caused by capacitance and/or inductance implying that R and X have to be summed up as vectors at right angles to each other to give (Z), see figure 8 where X_L is the inductance component and X_C is the capacitance component of reactance X.

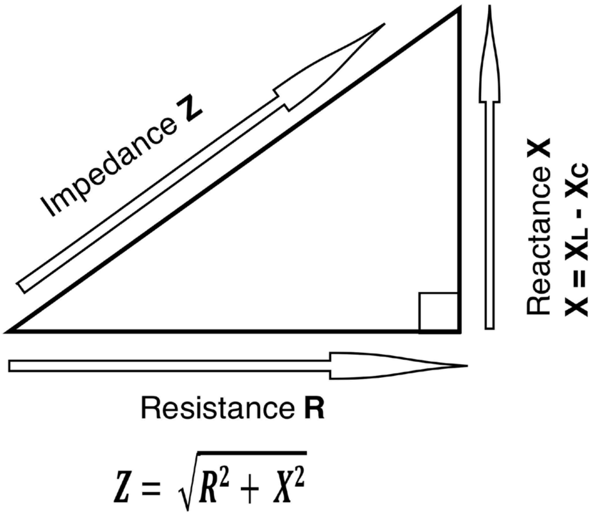

Figure 13: Illustration of the vector addition of resistance and reactance to give the impedance.

The relation between Z' and Z" as used in the complex plane plot is:

Equation 17 $$\left[Z' - {}^{R}\!/_{2}\right]^2 + (Z'' - 0)^2 = \left[{}^{R}\!/_{2}\right]^2$$

It should be noted that it's not always possible to observe three semicircles representing the three components of the polycrystalline sample, as some may not be expressed in the frequency range selected for the experiment. The capacitances of the associated resistances are usually used to classify the resistances as grain bulk resistance (~10^{-12} F), grain boundary resistance (10^{-11}-10^{-8} F), sample-electrode-interface resistance (10^{-7}-10^{-5} F) and electrochemical reactions (10^{-4} F).

The conductivity (σ) of a sample extracted from fitting of EIS data is often plotted by, taking its logarithmic value as a function of 1/T. The values are always normalized for the samples dimensions by equation 18.

Equation 18 $$\sigma\,(Scm^{-1}) = \frac{T(cm)}{R(\Omega) * A(cm^2)}$$

The elements commonly used to model the electrical resistance of solid electrolytes are namely, the resistor, the capacitor, the constant phase element and the inductor.

- **Resistor:** When current flows through it, it produces a voltage proportional to the flowing current with both the voltage and current being in sync (in phase) hence contributing only to the real part of the impedance. Its units are ohms, Ω.
- **Capacitor:** When a voltage is applied across a capacitor a current is produced that is proportional to the rate of change of the voltage across its terminals. The area and the length between two plates and the dielectric medium between them determine the capacitance whose units are in Farads, F. Since it stores energy and releases it when we stop applying a voltage it can impart a voltage lag of 90° behind the AC current therefore contributing to the imaginary part of the impedance.
- **Inductor:** it generates a voltage across each element proportional to the rate of change of a current flowing through it. When there is a coil on the circuit a magnetic field that induces a voltage across the conducting coiled part of the circuit is produced in the coil's centre. The induced voltage precedes the current by 90° thereby contributing to the imaginary part of the impedance known as the reactance. It is commonly found near the origin of the complex plane plot as a tail and is mainly due to the inductance in the wiring of the setup. It has units of Henries, H.
- **Constant phase element (CPE):** Is a general circuit element necessitated by the need to account for inhomogeneity of the system due to grain-boundaries, grain sizes and surface roughness among others and is its impedance can be defined as $Z = \frac{1}{Y} = \frac{1}{Y_0\,(j\omega)^n}$ where Y_0 has the numerical value of 1/|Z| at ω=1 rad/s, ω is frequency and n assumes any value between -1 and 1.For n=-1 it describes a pure CPE, for n=1 a pure resistor and for n=0 a pure inductor.

A Probostat© impedance cell from Norecs® coupled to a Solartron® 1260 frequency response analyser was used in the 2 probe impedance measurements. Experiments were run from between 150-1000 °C in steps of 50 °C in either wet or dry atmosphere. Typical gas atmospheres used were argon gas and oxygen gas. Occasionally 5%H_2 in Ar was used, keeping in mind the detrimental effects of hydrogen embrittlement on the Pt electrodes used in the experiments. Bubbling through water at room temperature generated wet gas while dry gas was generated by passing gas through two bottles of P_2O_5 before entering the cell. Typically an AC voltage of 1V rms and a frequency range of 1Hz-1MHz were used in measurements.

4.3 In-situ Characterization Techniques

A major challenge to solid electrolyte research has been the absence of sample cells designed to run multiple characterizations during one experiment such as impedance and neutron diffraction or in-situ hydration combined with powder diffraction. Therefore the development and testing of two in-situ cells for conducting simultaneous conductivity or hydration/gas-solid reactions with neutron powder diffraction as a function of temperature is demonstrated for proton conductors.

These techniques are defined by their ability to observe the phenomenon of interest as it occurs and in simulated real life conditions. Typically they comprise of a specially built sample environment cell that is mounted in a rig that facilitates the characterization of the sample under a given set of conditions while observing the phenomena of interest using one or more experimental techniques. In the case where two probing methods are used, the data sets are in-sync in terms of the timescale and experimental conditions (T, partial pressure etc.) experienced.

In this thesis, *in-situ* impedance measurements as a function of temperature are performed while simultaneously collecting neutron diffraction data from a sample of a proton conducting perovskite. Secondly, the hydration and dehydration behaviour of the material is investigated using neutron diffraction with a D_2O bearing gas as a function of temperature. This setup that can also be used to investigate oxide ion conductors under controlled $p(O_2)$. A further advantage of this approach is that all the data collected will be from just one sample and not different batches or pellets of the sample, so effects attributable to microstructure for example are the same over all the experiments and the samples experimental conditions are identical. The two separate setups designed for use at the ISIS beam lines are discussed below.

4.3.1 *In-situ* humidification setup

This consists of the gas flow cell [95] coupled to a gas humidification system which is itself connected to a gas mixing system as illustrated in figure 14 below whose components are named in table 1 in the appendix. The gas mixing system makes use of mass flow meters and precise pressure regulators that allow for simultaneous precision mixing of four gasses, currently O_2, Ar, CO_2, and CO. This allows for the precise setting of the oxygen partial pressure, $p(O_2)$, of the inlet gas. The *in-situ* gas flow cell consists of an oxygen sensor (3), which is positioned directly above the sample (10), usually in the form of porous pellets that are stacked on the quartz frit (11), and below is a thermocouple (12). The gas feed (13) is at the bottom of the quartz cell and the outlet at the top (1). The inlet is connected to the H_2O/D_2O injector (7) and gas mixing system (8). The furnace setup surrounds the narrower bottom part of the cell and consists of an electrical heating element (15) surrounded by three heat shields (14) all of which are made of thin vanadium sheets.

The gas humidification system (7) consists of a thermally insulated gas-washing bottle partially filled with D_2O and covered with a heating cord so that the contents can be kept at a constant set temperature. Through ball valves, the liquid content can be refilled by, blocking the gas inlet/outlet and opening alternate liquid input/output injection via a syringe. This provides the wet gas (6) to the *in-situ* cells.

A thermocouple inside the bottle linked to a temperature controller sets the required temperature of the contents allowing the $p(D_2O)$ to be controlled. A valve before the bottle allows dry gas to bypass the setup completely making it easy to switch between a humid and a dry gas flow (5).

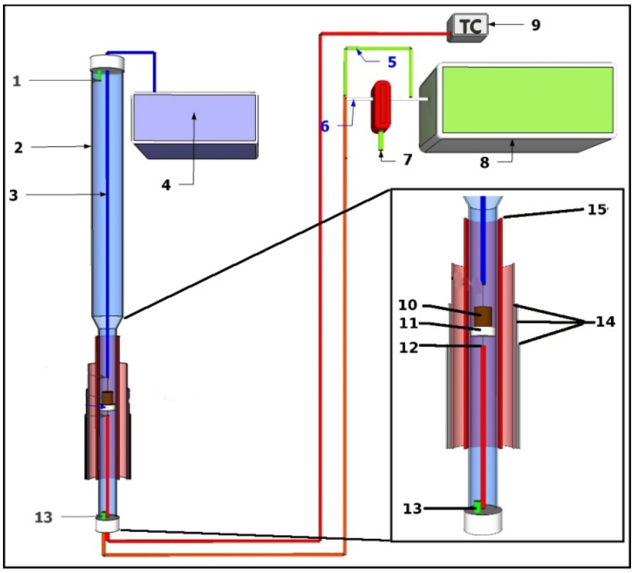

Figure 14: The high temperature *in-situ* humidification cell setup. The components are named in Table 1. Reproduced with permission from [96].

4.3.2 *In-situ* impedance spectroscopy setup

The *in-situ* impedance spectroscopy cell [97], see figure 15, whose components are named in table 2 in the appendix, consists of Pt electrodes (12) positioned in a recessed cavity inside two boron nitride (BN) shields (8,10), with platinum mesh added to ensure good contact. These elecrodes are springloaded and the electrical leads are also shielded by BN (14). The sample pellet (9) is positioned between two BN shields (8,10) such that diffration occurs only from the sample and not the hidden electrodes. A thermocouple (4) connected to a temperature controller (17) sits embeded within the bulk of the upper BN sample shield (8) in which the Pt electrical leads are embeded.

The furnace consists of an inner electrical heating element (13) and three outer heat shields (11) all made of thin vanadium sheets at the centre of which lies the quartz tube (3) bearing the mounted sample assembly. There is a gas inlet (15) and outlet (2) that can be used to supply and evacuate the cell as required. A Solartron S-1260 frequency response analyser (1) is coupled to the cells Pt leads and is used to collect impedance data. The gas inlet is connected to the gas mixing system (16). A series of tight fitting heat radiation baffles (5 - 7) ring the central support column. The sample is mounted and tightly held between the BN shields with the electrodes (faces) hidden from the neutrons but the side exposed to neutrons. The whole setup is then inserted into the neutron beam line.

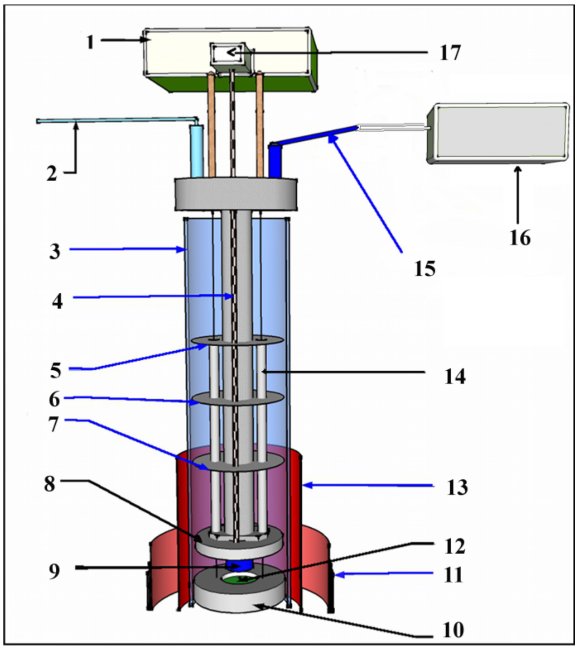

Figure 15: Schematics of the *in-situ* impedance spectroscopy cell. The components are named in Table 2. Reproduced with permission from [96].

5. Results and Discussion

In this section a brief summary of the main findings presented in the appended papers is given.

5.1 Improved proton conductivity through the co-doping of $BaZr_{0.5}In_{0.5}O_{3-\delta}$ with Yb^{3+}

Solid-state synthesis (SSS) and wet chemical preparation (WCR) of pure, $BaZr_{0.5}In_{0.5}O_{3-\delta}$, in which half of the In^{3+} was substituted for Yb^{3+} was performed. Pure cubic, perovskite type $BaZr_{0.5}In_{0.25}Yb_{0.25}O_{3-\delta}$ was obtained using the wet chemical route unlike in the SSS method whereby $Ba_3Yb_4O_9$, an impurity phase, was detected. The unit cell was found to have expanded on hydration compared to the dried sample, which was an indication of vacancy filling, by OH groups. This was confirmed by TGA that demonstrated the full filling of the vacancies in the sample on pre hydration at 300 °C. The composition of the cations in the sample was confirmed to be as expected within experimental error using EDX at 4:1:1:2 for Ba^{2+} In^{3+} Yb^{3+} and Zr^{4+} respectively.

Proton conductivity dominated below 600 °C in wet Ar gas conditions. This was further proven by the use of D_2O humidified gas stream whereby the deuteron conductivity was found to be lower than that of protons as expected and the value of the isotope effect was $\frac{\sigma_H}{\sigma_D} = 1.7$ vs. $\sqrt{2}$ for the classical isotope effect in close agreement with the findings according to Nowick *et. al.*[98] thereby demonstrating the isotope effect. The activation energies were, 0.44 eV for bulk conductivity, in agreement with common literature values of 0.4-0.5 eV[29, 99], while for the total conductivity it was 0.63 eV, below 350 °C in wet Ar indicating slower migration of protons across the grain boundaries.

The conductivity of $BaZr_{0.5}In_{0.25}Yb_{0.25}O_{3-\delta}$ was found to be greater than the singly doped $BaZr_{0.5}In_{0.5}O_{3-\delta}$ [68] and $BaZr_{0.5}Yb_{0.5}O_{3-\delta}$ [19]systems below 300 °C. Through co-doping the grain boundary conductivity and hence the total conductivity was increased compared to the singular doped systems, in agreement with the findings of Imashuku *et. al.*[100]. Additionally $BaZr_{0.5}In_{0.25}Yb_{0.25}O_{3-\delta}$ was found to undergo 100% filling of the vacancies created by doping compared to $BaZr_{0.5}Yb_{0.5}O_{3-\delta}$ after several days of hydration.

5.2 Spark plasma sintering of $BaZr_{0.5}In_{0.5}O_{3-\delta}$

The conductivity of $BaZr_{0.5}In_{0.5}O_{3-\delta}$ was investigated using EIS by comparing the conductivity of a pellet prepared by solid state sintering (SSS) and a spark plasma sintered (SPS) pellet obtained from the same powder. Powder X-ray diffraction showed the existence of a single phase in the SSS sample while the SPS processed sample had trace impurity peaks that disappeared once the sample was heated to 1500 °C in air. The main phase was indexed as cubic $Pm\bar{3}m$. The impurity in the SPS sample originated from the graphite die used, which served as a source of carbon that reacted with the sample on heating at 700 °C to remove the graphite. This resulted in the formation of $BaCO_3$, hence segregation of the ZrO_2 and In_2O_3 due to barium deficiency. However, when the SPS sample was heated to 1500 °C, the three components reacted to yield a single phase of the desired material with no impurities. A mass loss during TGA in the isothermal step at 900 °C which was attributable to the loss of carbon based species given SPS processing was in a graphite die.

Conductivity wise, wet hydrogen atmosphere exhibited the highest bulk and total protonic conductivity in the region of 150-600 °C compared to wet argon and dry Ar atmospheres for the SPS sample. The bulk and total conductivities for wet argon runs were slightly lower than those of prehydrated sample on heating under dry Ar, see figure 16b.

The activation energies (150–350 °C, figure 16b) of total conductivity samples containing protons were in the range of 0.36–0.62 eV and consistent with typical protonic conduction activation energies, 0.4-0.5 eV, of the best proton conductors, Y-doped $BaZrO_3$ or $BaCeO_3$ [30, 101]

For comparison data from SSS (1500 °C) [68] samples and sol gel synthesis (SOL 1100 °C) [68] was plotted together with SPS conductivity data showing that both bulk and total conductivity values for SPS sample in wet hydrogen were the highest, figure 17a. Protonic conductivity was in the order SPS ≈ SOL > SSS see figure 17b.

Under dry argon atmosphere for prehydrated samples, on heating the effect of the microstructure on conductivity was exposed. Conductivity in dry Ar heating followed the following trend SSS > SPS > SOL. This replicated grain size behaviour.

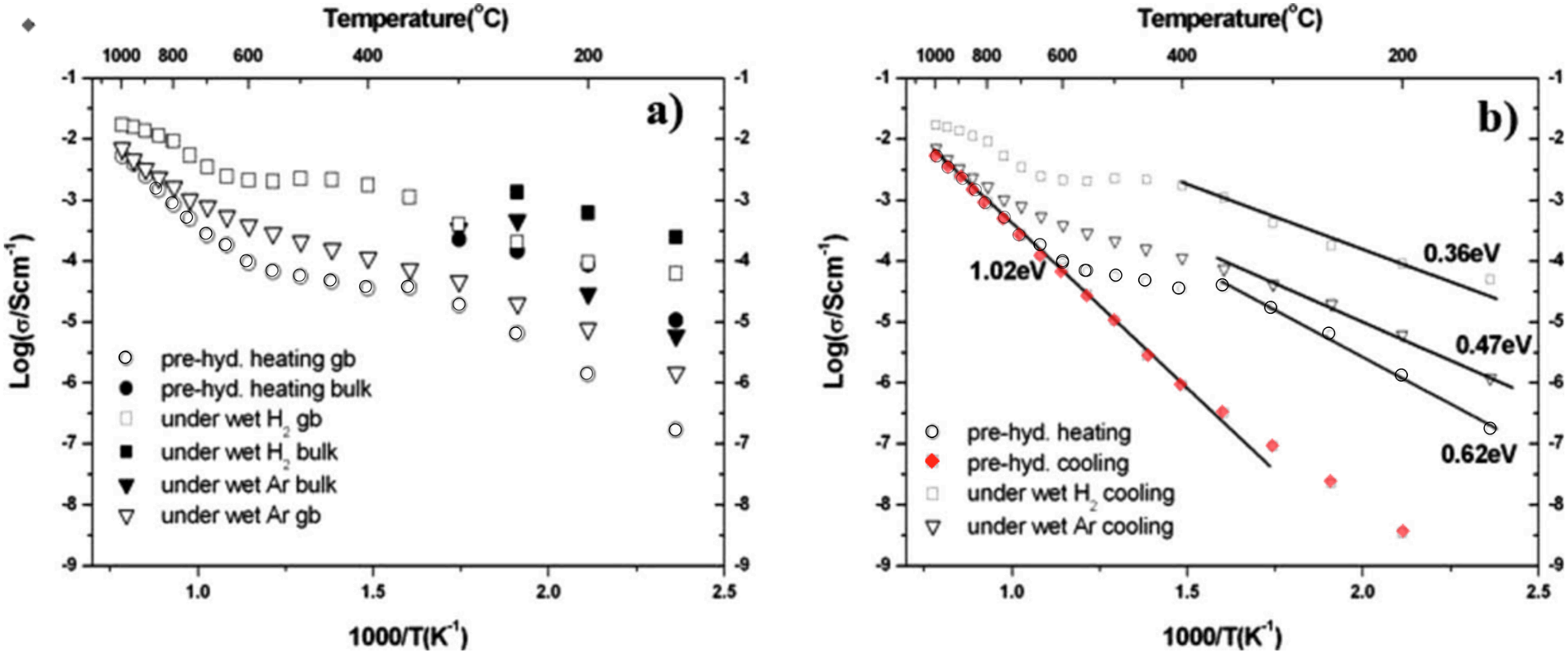

Figure 16: Conductivity of SPS $BaZr_{0.5}In_{0.5}O_{3-\delta}$ sample under different atmospheres (a): bulk and grain boundary (gb) and (b): total.

Reproduced with permission from [20]

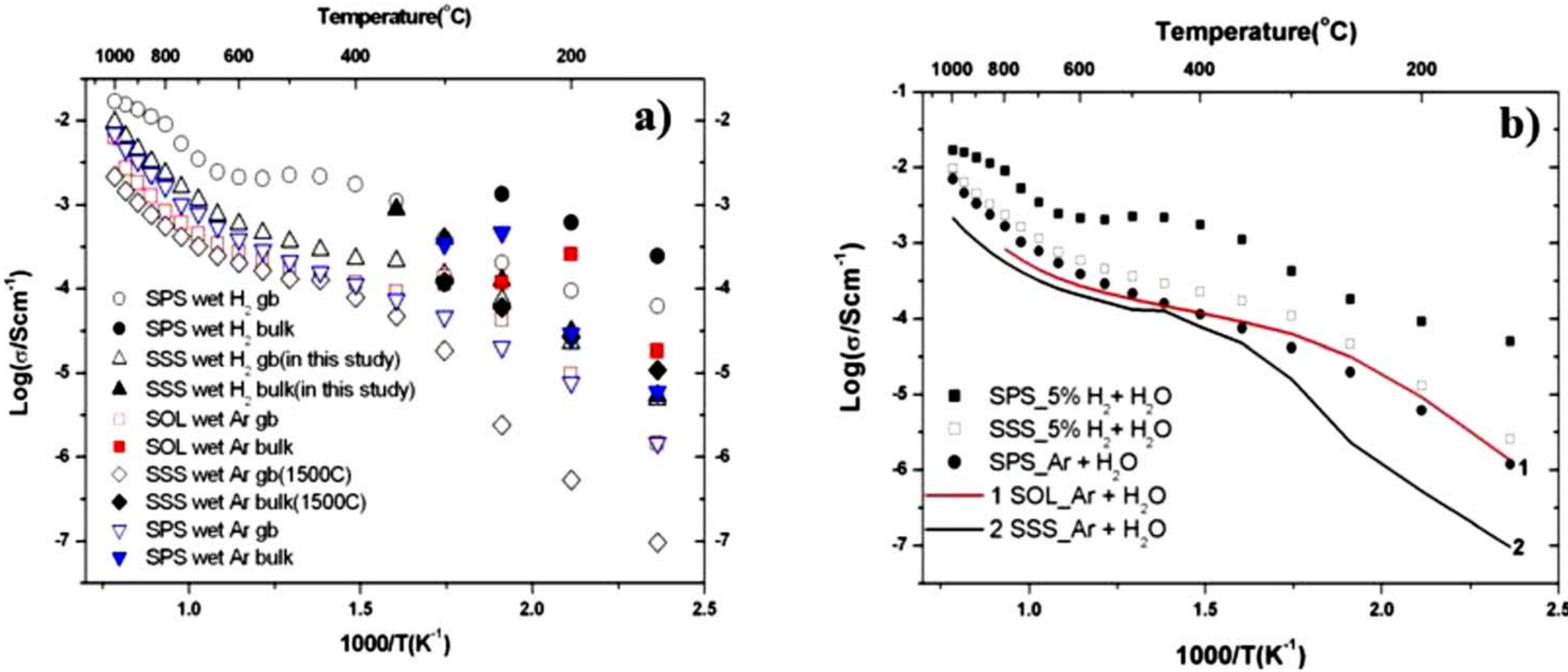

Figure 17: Comparison of (a) bulk and grain-boundary (gb) NB: SSS sample prepared in this paper is included (b) total conductivity under humid atmospheres. Data for SSS (1500 °C), SOL, and 1–2 have been taken from Ref [68]. Reproduced with permission from [20]

5.3 The *In-situ* conductivity and hydration studies using neutron powder diffraction

In this paper we reported the development of novel facilities for in-situ neutron powder diffraction studies of proton conducting ceramics using samples of $BaZr_{0.5}In_{0.5}O_{3-\delta}$ to demonstrate the equipment. The facilities allow for the in-situ hydration or exposure to a gas stream with variable oxygen partial pressure $p(O_2)$ and alternatively in-situ impedance measurements of samples pre-treated with deuterium (i.e. pre-deuterated). A dense pellet was made by pressing it under 8 tons of pressure for impedance measurements while less dense pellets were pressed at 4 tons of pressure for the in-situ hydration experiment.

From the in-situ hydration studies it was found that whenever the sample was in a hydrated (with deuterium, i.e. deuterated) state, it consisted of two phases, one with deuterons incorporated in the structure and the other phase containing no deuterons in it. The deuterated phase itself was approximately 80% deuterated (i.e. $BaZr_{0.5}In_{0.5}O_{2.75}$ $(D_2O)_{x.}$, $x = 0.20$) below 500 K. On cycling between the deuterated and dry state, hysteresis was observed in the cell parameter, a, the D_2O fraction and perhaps most surprisingly, the anisotropic thermal parameter u_{11} for oxygen and not in the u_{22} (u_{33}) parameter. The latter will perhaps be the subject of further investigation to help elucidate an explanation for the cell volume expansion linked to hydration.

In the impedance measurements of the hydrothermally deuterated sample, it was discovered that only one phase existed indicating the complete deuteration of the sample from the hydrothermal route employed. The conductivity of the in-situ sample was found to be an order of magnitude lower than reported values where a H_2O gas stream was used to hydrate the sample, an effect primarily associated with the isotope effect [98, 102]

5.4 Structure and conductivity of $BaSn_{0.6}Sc_{0.4}O_{3-\delta}$

$BaSn_{1-x}Sc_xO_{3-\delta}$ was synthesized for the series x = 0, 0.1, 0.2, 0.3, and 0.4 by the solid-state synthesis route. Except for $BaSnO_3$ and deuterium treated $BaSn_{0.6}Sc_{0.4}O_{3-\delta}$, the samples were found to exhibit complex phase behaviour composing of scandium rich and scandium poor phases in addition to Sc_2O_3 impurity. Hence we limited the discussion to the pure $BaSnO_3$ and the vacuum dried and deuterated $BaSn_{0.6}Sc_{0.4}O_{3-\delta}$. The samples were characterized by XRPD, EIS, NPD, and ^{119}Sn-NMR techniques. Room temperature neutron powder diffraction (NPD) data was collected for the samples. The deuterium treated $BaSn_{0.6}Sc_{0.4}O_{3-\delta}$ sample was used to locate the deuteron site in the unit cell at the crystallographic 24*k* site with $x = 0.58(1)$ and $y = 0.22(1)$, which give an average O-D bond distance of 0.96(1) Å.

^{119}Sn-NMR confirmed that D_2O dissolved into the structure of the dried sample. The results indicated that locally Sn^{4+} was surrounded by six Sn^{4+} in its first cation coordination shell *i.e.* $Sn(OSn)_6$, in $BaSnO_3$ as expected. However the same type of local environment persisted in $BaSn_{0.6}Sc_{0.4}O_{3-\delta}$ to a weaker extent in addition to a broader resonance tentatively assigned to Sn^{4+} environments with 5 Sn^{4+} and 1 Sc^{3+} in their 1st cation coordination sphere.

The activation energy of the bulk conductivity obtained by least square fitting of the linear region below 250 °C was found to be 0.43 eV close to values reported for $BaSn_{1-x}Y_xO_{3-\delta}$ [103] of between 0.34-0.41 eV while the total protonic conductivity activation energy lay in the 0.67-0.70 eV range, much lower than that of $BaSn_{0.875}Sc_{0.125}O_{3-\delta}$ (0.87 eV) [41] but much closer to that of $BaSn_{0.75}Sc_{0.25}O_{3-\delta}$ (0.73

eV) [104] most likely due to the higher doping concentration that enhanced the grain growth [103, 104].

The conductivity at 600 °C in wet Ar was 1.07×10^{-3} S cm^{-1} similar to that of $BaIn_{0.8}Ti_{0.2}O_{2.6}$ [105]. For related perovskites phases with lower substitution levels, e.g. $BaSn_{0.875}Y_{0.125}O_{3-\delta}$ [41] and $BaZr_{0.9}Sc_{0.1}O_{3-\delta}$ [66], the proton conductivity is reported to lie at ~ 5×10^{-4} S cm^{-1} suggesting the higher doping level increases proton conductivity. Most likely this trend reflects the greater proton concentration in our more highly doped system.

5.5 Proton conduction in oxygen deficient $Ba_3In_{1.4}Y_{0.3}M_{0.3}ZrO_8$ perovskites (M=Ga^{3+} or Gd^{3+})

B-site disordered, oxygen deficient $Ba_3In_{1.4}Y_{0.3}M_{0.3}ZrO_8$ (M = Gd^{3+} or Ga^{3+}) perovskites of space group $Pm\bar{3}m$, were prepared by a solid-state reactive sintering method. The samples were characterised using XRPD, TGA, EIS SEM and EDS. 79.3% and 55.5% population of the available oxygen vacancies were achieved on slow cooling in humidified N_2 gas from 400 °C. 74% and 88% relative densities were achieved for the Gadolinium containing sample and the Gallium containing sample respectively. The cell parameters were found to be 4.2487(1) Å and 4.2133(1) Å in the GdY:BIZO and GaY:BIZO respectively.

Under humid conditions and temperatures below 400 °C protons were found to be the dominant charge carriers regardless of the $p(O_2)$. Conductivity was found to be in the range of 1.7 - 6.7 × 10^{-4} S cm^{-1} ($M = Gd^{3+}$) and 0.9 - 3.79 × 10^{-4} S cm^{-1} ($M = Ga^{3+}$) for the temperature interval 300 to 700 °C. Hole conduction was observed by comparing conductivity under dry oxygen gas to that under dry argon gas with the expected observation being that if hole conduction was present then the conductivity under dry oxygen would be higher than in dry argon. Conductivity in dry oxygen was consequently found to be higher than in argon gas above 200 °C for both samples. The contribution of hole conduction in the GdY:BIZO was found to be half an order of magnitude less than that of GaY:BIZO above 400 °C. Hole conduction occurs due to equation 8,

Equation 19. $$\tfrac{1}{2}O_{2\,(g)} + V_O^{\bullet\bullet} = O_O^{x} + 2h^{\bullet}$$

Although the density of the GdY:BIZO (74%) was lower than that of GaY:BIZO (88%), its conductivity was ~50% higher in the temperature region of 400 °C to 550 °C under wet Ar gas conditions. The oxide ion conductivity at 1000 °C, i.e. conductivity under dry Ar, was found to be approximately twice more in GdY:BIZO compared to GaY:BIZO which was rationalized to be due to the larger unit cell of GdY:BIZO brought about by Gd^{3+} doping.

5.6 Pyrochlore - Fluorite Transition in $Y_2(Ti_{1-x}Zr_x)_2O_7$ $(0.0 \leq x \leq 1.0)$

Samples of $Y_2(Ti_{1-x}Zr_x)_2O_7$ for x=0.00, 0.15, 0.30, 0.40, 0.50, 0.65 and 0.80 were synthesized using the SSS method using the pre-dried oxides. The densities achieved for the samples ranged from 65% to 70%.

The grain boundary conductivities for all the samples lay in the range $1\text{-}3\times10^{-6}$ S cm^{-1} and were largely independent of the temperature unlike the bulk conductivities. Samples with $x \leq 0.3$ were found to have a bulk conductivity that varied in a linear fashion with temperature, as were those with compositions of $x \geq 0.3$ except for temperatures above 1000 K.

Plotting the conductivity versus composition revealed that there was an initial jump in conductivity over the range $0.00 \leq x \geq 0.4$ of at least approximately an order of magnitude before the conductivity plateaued out at higher x values. This was followed by a small increase at x =1.0 whose data was obtained from a previous study[106].

To explain this behaviour Rietveld refinements, and thereafter, total scattering analysis were undertaken. The starting point was $Y_2Ti_2O_7$ was modelled in the $Fd\bar{\bar{3}}m$ space group with a lattice parameter a ~10.1 Å with Y^{3+} occupying the A-site with a distorted cubic environment, while Ti^{4+} occupied a distorted octahedral environment at the B-site. On examining the neutron diffraction patterns, some Bragg peaks were found to broaden at x = 0.65 and disappear at x =0.80 consistent with a pyrochlore-disordered fluorite transition. Rietveld refinements performed included a variation of the scattering lengths over the two crystallographic distinct cation positions as it was impossible to reliably determine the three cations' distributions over the two sites for $x > 0.0$. The results of the Rietveld refinements were used to generate the starting models for the detailed reverse Monte Carlo (RMC) analysis of the total neutron scattering data (The intricacies of the RMC method are beyond the scope of this thesis).

As a result it was found that Zr^{4+} initially entered the B-site exclusively replacing Ti^{4+} adopting a cubic rather than octahedral environment. At concentrations in excess of x=0.4 there was an increasing tendency of the three cations to disorder over the A-site and B-site which was complete at 0.85. This was accompanied by the redistribution of the oxygen anion initially involving those on the 48*f* site.

In terms of co-ordination numbers, in brackets, Ti^{4+} (6) co-ordination number was found to steadfastly prefer a six-coordination state with increasing x while that of Y^{3+} (8) gradually decreased. Zr^{4+} (~6) which is initially at the same B-site as Ti^{4+} (6) increases steadily with x to a slightly lower value than that of Y^{3+} at x=1, a fact that is most likely due to the preference of anion vacancies to be preferentially located as nearest neighbour to the smaller cation within zirconia based oxides [107].

Increasing the value of x still resulted in the Y^{3+} and Ti^{4+} retaining their cubic and distorted octahedral environments respectively even though Y^{3+} coordination number decreased as some vertices becoming vacant as the anions move to the vacant anion site. Given that the Zr^{4+} initially enters the Ti^{4+} site its preference for a cubic environment albeit with some of the vertices vacant results in a significant increase in the degree of disorder within the anion sub-lattice.

Hence it becomes evident that the initial preference of Zr^{4+} for the Ti^{4+} site on substitution and its preference for a cubic local environment results in a degree of disorder in the anion sub lattice, as vacancies tend to associate with it, hence the initial jump in conductivity. The dramatic disordering of the cations over the A-site and B-site accompanied by the displacement of a significant number of anions into the vacant anion site at higher x values does not significantly alter the conductivity.

Conclusion and Future Work

In Paper I the importance of investigating the effects of co-doping has been demonstrated. The results indicate a positive effect of Yb as a co-dopant in In:$BaZrO_3$. In paper II the various synthesis and processing techniques of $BaZr_{0.5}In_{0.5}O_{2.75}$ have been elaborated in relation to the microstructure, which has been shown to affect the behaviour of conductivity. The achievement of a high level of densification via SPS is demonstrated and the need for long soaking times to achieve large grains is demonstrated.

Paper III has demonstrated the *in-situ* experimental characterization facilities at ISIS developed in partnership with Chalmers University of Technology using a well-known system of $BaZr_{0.5}In_{0.5}O_{2.75}$. The additional new insight into the hydration behaviour with respect to temperature and the structural thermal parameters of the oxygen anion has been gained in this work. Further studies of the hydration behaviour of other proton conducting perovskites, e.g. $BaCe_{0.8}Y_{0.2}O_{3-\delta}$, are now underway which show significant effect of $p(D_2O)$ on the structural transition temperatures in the material. So far scientists from all over the world have used the two *in-situ* cells in a total of 14 experiments.

In the fluorite-pyrochlore O^{2-} conducting system, $Y_2(Ti_{1-x}Zr_x)_2O_7$, paper IV, it has been demonstrated that Zr favours the substitution of the Ti site for lower Zr content resulting in the initial jump in conductivity as a function of Zr content which brings about the anion disordering hence increasing the oxide ion conductivity. At higher Zr substitutions there is a gradual disordering of the cations over the cation sites that is associated with a much smaller jump in conductivity. The tuning of the anion disordering in the fluorite-pyrochlore system should be further investigated as an avenue of improving oxide ion conduction.

In paper V, we have demonstrated the surprising finding of having an order of magnitude higher conductivity in oxidizing conditions for GaY;BIZO compared to GdY:BIZO for such a small percentage Ga on the B-site (15%) in the oxygen deficient perovskite. The two systems are ideally compatible and in the future GdY:BIZO could possibly be used an electrolyte once its sinterability is addressed while GaY;BIZO is used as the mixed conducting cathode material

A detailed understanding on $BaSn_{0.6}Sc_{0.4}O_{2.8}$ (paper VI) has been developed and the deuteron site plus a detailed atomic model obtained. The contrast between the various probing techniques such as XRPD, NPD and NMR and the complimentary information they provide was demonstrated. Further, this material also possesses electronic conductivity and hence can in the future be applied as a cathode material for fuel cells.

In the future a more detailed understanding of the proton conducting oxygen deficient perovskites ability to have enhancement or suppression of the hole conductivity would be investigated. The results of experiments using the in-situ gas flow cell on $Ce_{0.5}Zr_{0.5}O_2$ and the $FeMnO_3$ system will be presented in the future.

Acknowledgements

Many thanks and gratitude and thanks to my supervisor, Professor Sten Eriksson for his unwavering support, guidance, teaching, encouragement and trust throughout my PhD work and together with Professor Emeritus, Oliver Lindqvist, say thank you for enabling my studentship at the Environmental Inorganic Chemistry division at Chalmers University of Science and Technology. I thank my examiner Professor Jan-Erik Svensson for facilitating sufficient time for the completion of the thesis.

Appreciation goes to my co-supervisors Associate Professors Stefan Norberg and Chris Knee, for their invaluable discussions, suggestions and input into my research. Sincere gratitude goes to Dr. Istaq Ahmed for being a mentor and a role model and for the many informal discussions.

Thanks to members of the oxide group both current and former, including Dr. Annika Eriksson, Habibur Rahman and Stefan Saxin for making life in the office and in the labs lively and a breeze. Special thanks to Professor Vratislav Langer, support personnel Roger Saghdahl and Esa Väänänen without whom my experiments would not be possible.

A special mention goes to Professor Elisabet Ahlberg and Dr. Patrick Steegstra of the Electrochemistry group at Gothenburg University for their expert advice, collaboration and troubleshooting in their labs when things got tough.

Much appreciation goes to collaborators Dr. Steve Hull of the ISIS facility in Oxford, U.K for his expertise in Neutron diffraction and Dr. Lucienne Buannic, Dr. Frédéric Blanc and Professor Clare P. Grey of Stony Brook University in N.Y, USA and University of Cambridge, U.K. for their invaluable input in NMR studies.

I deeply acknowledge the Swedish research council for the financial support in my work and the possibility of obtaining neutron beam time.

Finally to my wife, Wanja, and Family whom without their understanding, love and support the writing of this thesis would not have been accomplished.

Francis Kinyanjui

Gothenburg, September 2013

Appendix

Table 1: Key descriptors of the *in-situ* humidification cell

	Description
1	Gas Outlet
2	Quartz tube
3, 10	Oxygen sensor
4	Oxygen sensor controller
5	Dry gas inlet
6	Wet gas inlet
7	Gas humidifier
8	Gas mixing setup
9	Temperature controller
10	Sample
11	Quartz fritz
12	Thermocouple
13	Gas inlet
14	Vanadium heat shields (3)
15	Vanadium heating element

Table 2: Key descriptors of the *in-situ* impedance spectroscopy cell

	Description
1	Solartron 1260
2	Gas Outlet
3	Quartz tube
4	Thermocouple
5-7	Heat radiation baffles
8, 10	Boron nitride (BN) shielding
9	Sample
11	Vanadium heat shields (3)
12	Platinum electrode
13	Vanadium heating element
14	BN shielding for electrode
15	Gas inlet
16	Gas mixing setup
17	Temperature controller

References

[1] R. Lee, "The outlook for population growth," *Science (New York, N.Y.),* vol. 333, pp. 569, Jul 29 2011.

[2] S. Institution. (2009, 2013/08/02). *Collecting the History of Alkali Fuel Cells*. Available: http://americanhistory.si.edu/fuelcells/alk/alkmain.htm

[3] F. C. Today. (2013, 2013/08/02). *Fuel Cell History* Available: http://www.fuelcelltoday.com/about-fuel-cells/history

[4] Wikipedia. (2013, 2013/08/02). *UTC Power - Wikipedia, the free encyclopedia*. Available: http://en.wikipedia.org/wiki/UTC_Power

[5] B. P. S. Inc. (2013, 2013/08/02). *Fuel Cell Products | Ballard Power Systems*. Available: http://www.ballard.com/fuel-cell-products/

[6] Bloomenergy. (2013, 2013/08/02). *ES-5700 Fuel Cell Data Sheet | Bloom Energy*. Available: http://www.bloomenergy.com/fuel-cell/es-5700-data-sheet/

[7] Y. Inui, T. Matsumae, H. Koga, and K. Nishiura, "High performance SOFC/GT combined power generation system with CO_2 recovery by oxygen combustion method," *Energy Conversion and Management,* vol. 46, pp. 1837, 2005.

[8] P. Jens, S. Azra, and S. Lars, "Combined solid oxide fuel cell and gas turbine systems for efficient power and heat generation," *Journal of Power Sources,* vol. 86, pp. 442, 2000.

[9] B. F. Möller, J. Arriagada, M. Assadi, and I. Potts, "Optimisation of an SOFC/GT system with CO_2-capture," *Journal of Power Sources,* vol. 131, pp. 320, 2004.

[10] A. Elgowainy and M. Wang, "Fuel cycle comparison of distributed power generation technologies," Argonne National Laboratory, Argonne, Illinois ANL/ESD/08-4, November 2008.

[11] U. DoE. (2011, August 12). *Comparison of Fuel Cell Technologies*. Available: http://www1.eere.energy.gov/hydrogenandfuelcells/fuelcells/pdfs/fc_comparison_chart.pdf

[12] B. C. H. Steele and A. Heinzel, "Materials for fuel-cell technologies," *Nature,* vol. 414, pp. 345, 2001.

[13] T. H. Etsell and S. N. Flengas, "Electrical properties of solid oxide electrolytes," *Chemical Reviews,* vol. 70, pp. 339, Jul 1970.

[14] N. Q. Minh, "Ceramic Fuel Cells," *Journal of the American Ceramic Society,* vol. 76, pp. 563, Apr 1993.

[15] T. Norby, "The promise of protonics," *Nature,* vol. 410, pp. 877, Apr 19 2001.

[16] D. A. Boysen, T. Uda, C. R. I. Chisholm, and S. M. Haile, "High-Performance Solid Acid Fuel Cells Through Humidity Stabilization," *Science,* vol. 303, pp. 68, January 2 2004.

[17] S. M. Haile, D. A. Boysen, C. R. I. Chisholm, and R. B. Merle, "Solid acids as fuel cell electrolytes," *Nature,* vol. 410, pp. 910, 2001.

[18] I. Ahmed, S. G. Eriksson, E. Ahlberg, C. S. Knee, M. Karlsson, A. Matic*, et al.*, "Proton conductivity and low temperature structure of In-doped BaZrO3," *Solid State Ionics,* vol. 177, pp. 2357, 2006.

[19] I. Ahmed, C. S. Knee, S. G. Eriksson, E. Ahlberg, M. Karlsson, A. Matic*, et al.*, "Proton conduction in perovskite oxide $BaZr_{0.5}Yb_{0.5}O_{3-\delta}$ prepared by wet chemical synthesis route," *Journal of The Electrochemical Society,* vol. 155, pp. P97, 2008.

[20] I. Ahmed, F. G. Kinyanjui, P. Steegstra, Z. J. Shen, S. G. Eriksson, and M. Nygren, "Improved proton conductivity in spark-plasma sintered dense ceramic $BaZr_{0.5}In_{0.5}O_{3-\delta}$," *Electrochemical and Solid-State Letters,* vol. 13, pp. B130, 2010.

[21] S. Tao and J. T. S. Irvine, "Conductivity studies of dense yttrium-doped $BaZrO_3$ sintered at 1325 °C," *J. Solid State Chem.,* vol. 180, pp. 3493, Dec 2007.

[22] M. M. Bucko, "Ionic conductivity of the yttria-stabilized-zirconia nanomaterials," in *9th IEEE Conference on Nanotechnology*, Genoa, pp. 543.

[23] P. Babilo and S. M. Haile, "Enhanced Sintering of Yttrium-Doped Barium Zirconate by Addition of ZnO," *Journal of the American Ceramic Society,* vol. 88, pp. 2362, Sep 2005.

[24] O. J. Durá, M. A. López de la Torre, L. Vázquez, J. Chaboy, R. Boada, A. Rivera-Calzada*, et al.*, "Ionic conductivity of nanocrystalline yttria-stabilized zirconia: Grain boundary and size effects," *Physical Review B,* vol. 81, pp. 184301, June 2010.

[25] K. D. Kreuer, S. Adams, W. Münch, A. Fuchs, U. Klock, and J. Maier, "Proton conducting alkaline earth zirconates and titanates for high drain electrochemical applications," *Solid State Ionics,* vol. 145, pp. 295, Dec 2001.

[26] R. Glöckner, M. S. Islam, and T. Norby, "Protons and other defects in BaCeO3: a computational study," *Solid State Ionics,* vol. 122, pp. 145, Oct 1999.

[27] J. M. Peter, N. T. Barry, and B. N. David, "CODATA recommended values of the fundamental physical constants: 2006," *Reviews of Modern Physics,* vol. 80, 2008.

[28] K.-D. Kreuer, "Proton Conductivity: Materials and Applications," *Chemistry of Materials,* vol. 8, pp. 610, Mar 1996.

[29] K. D. Kreuer, "Aspects of the formation and mobility of protonic charge carriers and the stability of perovskite-type oxides," *Solid State Ionics,* vol. 125, pp. 285, Oct 1999.

[30] K. D. Kreuer, "PROTON-CONDUCTING OXIDES," *Annual Review of Materials Research,* vol. 33, pp. 333, 2003.

[31] I. Ahmed, "Acceptor-Doped BaZrO3 Perovskite: Synthesis, Structure and Proton Conductivity," Doctoral thesis

, Chemical and Biological Engineering Chalmers University of Technology, Göteborg, 2008.

[32] N. Bonanos, "Transport properties and conduction mechanism in high-temperature protonic conductors," *Solid State Ionics,* vol. 53-56, pp. 967.

[33] D. Ruzmetov, Y. Seo, L. J. Belenky, D. M. Kim, X. Ke, H. Sun, *et al.*, "Epitaxial Magnetic Perovskite Nanostructures," *Advanced Materials,* vol. 17, pp. 2869, Dec 05 2005.

[34] R. J. H. Voorhoeve, D. W. Johnson, J. P. Remeika, and P. K. Gallagher, "Perovskite Oxides: Materials Science in Catalysis," *Science,* vol. 195, pp. 827, Apr 04 1977.

[35] Y. Takeda, N. Imanishi, R. Kanno, T. Mizuno, H. Higuchi, O. Yamamoto, *et al.*, "Oxide ion conductivity in perovskite type Sr_2ScAlO_5 and related compounds," *Solid State Ionics,* vol. 53-56, pp. 748, 1992.

[36] T. Scherban, W. K. Lee, and A. S. Nowick, "Bulk protonic conduction in Yb-doped $SrCeO_3$ and $BaCeO_3$," *Solid State Ionics,* vol. 28-30, pp. 585, Sep 1988.

[37] X. Chu, "Dilute CH_3SH-sensing characteristics of $BaSnO_3$ thick film sensor," *Materials Science and Engineering B,* vol. 106, pp. 305, Feb 15 2004.

[38] U. Lampe, J. Gerblinger, and H. Meixner, "NITROGEN-OXIDE SENSORS BASED ON THIN-FILMS OF BASNO3," *Sensors and Actuators B: Chemical,* vol. 26, pp. 97, Jun 1995.

[39] J. Cerdà, J. Arbiol, G. Dezanneau, R. Díaz, and J. R. Morante, "Perovskite-type $BaSnO_3$ powders for high temperature gas sensor applications," *Sensors and Actuators B: Chemical,* vol. 84, pp. 21, 2002.

[40] "Characterization of BaSnO3-based ceramics-Part 1. Synthesis, processing and microstructural development," pp. 1, Jun 25 1998.

[41] Y. Wang, A. Chesnaud, E. Bevillon, J. Yang, and G. Dezanneau, "Synthesis, structure and protonic conduction of $BaSn_{0.875}M_{0.125}O_{3-\delta}$ (M = Sc, Y, In and Gd)," *International Journal of Hydrogen Energy,* vol. 36, pp. 7688, 2011.

[42] S. Upadhyay and P. Kavitha, "Lanthanum doped barium stannate for humidity sensor," *Materials Letters,* vol. 61, pp. 1912, Apr 2007.

[43] É. Bévillon, G. Geneste, A. Chesnaud, Y. Wang, and G. Dezanneau, "Ab initio study of La-doped $BaSnO_3$ proton conductor," *Ionics,* vol. 14, pp. 293, 2008.

[44] F. Kröger, "The Chemistry of Imperfect Crystals (1964)," *for a discussion of the question and further references,* p. 810, 1967.

[45] F. Kröger and H. Vink, "Relations between the concentrations of imperfections in crystalline solids," *Solid state physics,* vol. 3, pp. 307, 1956.

[46] I. Ahmed, S. M. H. Rahman, P. Steegstra, S. T. Norberg, S. G. Eriksson, E. Ahlberg, *et al.*, "Effect of co-doping on proton conductivity in perovskite oxides $BaZr_{0.9}In_{0.05}M_{0.05}O_{3-\delta}$ (M = Yb^{3+} or Ga^{3+})," *International Journal of Hydrogen Energy,* vol. 35, pp. 6381, 2010.

[47] I. Ahmed, F. G. Kinyanjui, S. M. H. Rahman, P. Steegstra, S. G. Eriksson, and E. Ahlberg, "Proton conductivity in mixed b-site doped perovskite oxide $BaZr_{0.5}In_{0.25}Yb_{0.25}O_{3-\delta}$," *Journal of The Electrochemical Society,* vol. 157, pp. B1819, 2010.

[48] H. Iwahara, T. Esaka, H. Uchida, and N. Maeda, "Proton conduction in sintered oxides and its application to steam electrolysis for hydrogen production," *Solid State Ionics,* vol. 3-4, pp. 359, 1981.

[49] K. Koji, K. Yoshirou, S. Tetsuo, and I. Hiroyasu, "Protonic conduction in Zr-substituted $BaCeO_3$," *Solid State Ionics,* vol. 138, pp. 91, 2000.

[50] H. G. Bohn and T. Schober, "Electrical conductivity of the high-temperature proton conductor $BaZr_{0.9}Y_{0.1}O_{2.95}$," *Journal of the American Ceramic Society,* vol. 83, pp. 768, Apr 2000.

[51] N. Zakowsky, S. Williamson, and J. Irvine, "Elaboration of CO_2 tolerance limits of $BaCe_{0.9}Y_{0.1}O_{3-\delta}$ electrolytes for fuel cells and other applications," *Solid State Ionics,* vol. 176, pp. 3019, 2005.

[52] V. B. Sanjeevani, "Stability of $BaCeO_3$-Based Proton Conductors in Water-Containing Atmospheres," *Journal of The Electrochemical Society,* vol. 146, p. 2038, 1999.

[53] T. Yajima, K. Koide, H. Takai, N. Fukatsu, and H. Iwahara, "Application of hydrogen sensor using proton conductive ceramics as a solid electrolyte to aluminum casting industries," *Solid State Ionics,* vol. 79, pp. 333, Jul 1995.

[54] F. E, D. A, D. E, L. S, and T. E, "Tailoring the chemical stability of $Ba(Ce_{0.8-x}Zr_x)Y_{0.2}O_{3-\delta}$ protonic conductors for Intermediate Temperature Solid Oxide Fuel Cells (IT-SOFCs)," *Solid State Ionics,* vol. 179, pp. 558, 2008.

[55] H. Park, C. Kwak, K. Lee, S. Lee, and E. Lee, "Interfacial protonic conduction in ceramics," *Journal of The European Ceramic Society,* vol. 29, pp. 2429, Sep 2009.

[56] Z. Sun, E. Fabbri, L. Bi, and E. Traversa, "Lowering grain boundary resistance of $BaZr_{0.8}Y_{0.2}O_{3-\delta}$ with $LiNO_3$ sintering-aid improves proton conductivity for fuel cell operation," *Physical chemistry chemical physics : PCCP,* vol. 13, pp. 7692, May 7 2011.

[57] S. W. Tao and J. T. S. Irvine, "A Stable, Easily Sintered Proton- Conducting Oxide Electrolyte for Moderate-Temperature Fuel Cells and Electrolyzers," *Advanced Materials,* vol. 18, p. 1581, Jun 19 2006.

[58] T. Jianhua, C. Daniel, H. Michael, and O. H. Ryan, "Cost-effective solid-state reactive sintering method for high conductivity proton conducting yttrium-doped barium zirconium ceramics," *Solid State Ionics,* vol. 181, pp. 496, 2010.

[59] S. Ricote and N. Bonanos, "Enhanced sintering and conductivity study of cobalt or nickel doped solid solution of barium cerate and zirconate," *Solid State Ionics,* vol. 181, 2010.

[60] T. Norby, "Solid-state protonic conductors: principles, properties, progress and prospects," *Solid State Ionics,* vol. 125, pp. 1, Oct 1999.

[61] E. Fabbri, L. Bi, D. Pergolesi, and E. Traversa, "Towards the next generation of solid oxide fuel cells operating below 600 °C with chemically stable proton-conducting electrolytes," *Advanced materials (Deerfield Beach, Fla.),* vol. 24, pp. 195, Jan 10 2012.

[62] H. Reidar and N. Truls, "Proton conduction in rare-earth ortho-niobates and ortho-tantalates," *Nature Materials,* vol. 5, pp. 193, 2006.

[63] H. Bohn, "The high temperature proton conductor $Ba_3Ca_{1.18}Nb_{1.82}O_{9-\delta}$. I. Electrical conductivity," *Solid State Ionics,* vol. 117, pp. 219, 1999.

[64] I. Ahmed, S. G. Eriksson, E. Ahlberg, C. S. Knee, H. Götlind, L. G. Johansson*, et al.*, "Structural study and proton conductivity in Yb-doped $BaZrO_3$," *Solid State Ionics,* vol. 178, pp. 515, Apr 2007.

[65] I. Ahmed, M. Karlsson, S. G. Eriksson, E. Ahlberg, C. S. Knee, K. Larsson*, et al.*, "Crystal Structure and Proton Conductivity of $BaZr_{0.9}Sc_{0.1}O_{3-\delta}$," *Journal of the American Ceramic Society,* vol. 91, pp. 3039, 2008.

[66] I. Ahmed, E. Ahlberg, S. Eriksson, C. Knee, M. Karlsson, A. Matic*, et al.*, "Structural study and conductivity of $BaZr_{0.90}Ga_{0.10}O_{2.95}$," Cocoa Beach, FL, 2006, pp. 105.

[67] I. Ahmed, C. S. Knee, M. Karlsson, S. G. Eriksson, P. F. Henry, A. Matic*, et al.*, "Location of deuteron sites in the proton conducting perovskite $BaZr_{0.50}In_{0.50}O_{3-y}$," *Journal of Alloys and Compounds,* vol. 450, pp. 103, 2008.

[68] I. Ahmed, S. G. Eriksson, E. Ahlberg, and C. S. Knee, "Influence of microstructure on electrical properties in $BaZr_{0.5}In_{0.5}O_{3-\delta}$ proton conductor," *Solid State Ionics,* vol. 179, pp. 1155, 2008.

[69] M. A. Subramanian, G. Aravamudan, and G. V. S. Rao, "Oxide pyrochlores - A review," *Progress in Solid State Chemistry,* vol. 15, pp. 55, 1983.

[70] M. Licia, W. G. Robin, and E. S. Kurt, "Disorder in Pyrochlore Oxides," *Journal of the American Ceramic Society,* vol. 83, pp. 1873, 2004.

[71] F. Jona, G. Shirane, and R. Pepinsky, "Dielectric, X-Ray, and Optical Study of Ferroelectric $Cd_2Nb_2O_7$ and Related Compounds," *Physical Review,* vol. 98, pp. 903, 1955.

[72] T. Dijk, V. J, and A. Burggraaf, "Electrical conductivity of fluorite and pyrochlore $Ln_xZr_{1-x}O_{2-x/2}$ (Ln = Gd, Nd) Solid Solutions," *Physica Status Solidi (a),* vol. 58, pp. 115, 1980.

[73] W. E. Klee and G. Weitz, "Infrared spectra of ordered and disordered pyrochlore-type compounds in the series $RE_2Ti_2O_7$, $RE_2Zr_2O_7$ and $RE_2Hf_2O_7$," *Journal of Inorganic and Nuclear Chemistry,* vol. 31, pp. 2367, 1969.

[74] L. Malavasi, C. A. J. Fisher, and M. S. Islam, "Oxide-ion and proton conducting electrolyte materials for clean energy applications: structural and mechanistic features," *Chemical Society Reviews,* vol. 39, pp. 4370, Nov 2010.

[75] O. Kwon and G. Choi, "Electrical conductivity of thick film YSZ," *Solid State Ionics,* vol. 177, pp. 3057, Nov 30 2006.

[76] K. Eguchi, T. Setoguchi, T. Inoue, and H. Arai, "Electrical properties of ceria-based oxides and their application to solid oxide fuel cells," *Solid State Ionics,* vol. 52, pp. 165, May 1992.

[77] S. Wang, "Nonstoichiometry of $Ce_{0.9}Gd_{0.1}O_{1.95-x}$," *Solid State Ionics,* vol. 107, pp. 73, 1998.

[78] S. Dae Jong, R. Kyoung Ok, P. Seung Bin, K. Ki Young, and S. Rak-Hyun, "Synthesis and properties of $Ce_{1-x}Gd_xO_{2-x/2}$ solid solution prepared by flame spray pyrolysis," *Materials Research Bulletin,* vol. 41, pp. 359, 2006.

[79] P. Shuk, H. D. Wiemhöfer, U. Guth, W. Göpel, and M. Greenblatt, "Oxide ion conducting solid electrolytes based on Bi_2O_3," *Solid State Ionics,* vol. 89, pp. 179, 1996.

[80] M. J. Verkerk, K. Keizer, and A. J. Burggraaf, "High oxygen ion conduction in sintered oxides of the Bi_2O_3-Er_2O_3 system," *Journal of Applied Electrochemistry,* vol. 10, pp. 81, 1980.

[81] R. Mukundan, P. Davies, and W. Worrell, "Electrochemical Characterization of Mixed Conducting $Ba(Ce_{0.8-y}Pr_yGd_{0.2})O_{2.9}$ Cathodes," *Journal of The Electrochemical Society,* vol. 148, p. A82, 2001.

[82] E. Fabbri, T.-k. Oh, S. Licoccia, E. Traversa, and E. Wachsman, "Mixed Protonic/Electronic Conductor Cathodes for Intermediate Temperature SOFCs Based on Proton Conducting Electrolytes," *Journal of The Electrochemical Society,* vol. 156, pp. B38, 2009.

[83] A. Magrasó, R. Haugsrud, M. Segarra, and T. Norby, "Defects and transport in Gd-doped $BaPrO_3$," *Journal of Electroceramics,* vol. 23, pp. 80, 2009.

[84] E. Fabbri, I. Markus, L. Bi, D. Pergolesi, and E. Traversa, "Tailoring mixed proton-electronic conductivity of $BaZrO_3$ by Y and Pr co-doping for cathode application in protonic SOFCs," *Solid State Ionics,* vol. 202, pp. 30, 2011.

[85] T. Schneller and T. Schober, "Chemical solution deposition prepared dense proton conducting Y-doped $BaZrO_3$ thin films for SOFC and sensor devices," *Solid State Ionics,* vol. 164, pp. 131, Nov 2003.

[86] U. Anselmi-Tamburini, M. T. Buscaglia, M. Viviani, M. Bassoli, C. Bottino, V. Buscaglia*, et al.*, "Solid-state synthesis and spark plasma sintering of submicron $BaY_xZr_{1-x}O_{3-x/2}$ (x=0, 0.08 and 0.16) ceramics," *Journal of the European Ceramic Society,* vol. 26, pp. 2313, 2006.

[87] S. Hull, R. I. Smith, W. I. F. David, A. C. Hannon, J. Mayers, and R. Cywinski, "The Polaris powder diffractometer at ISIS," *Physica B: Condensed Matter,* vol. 180-181, pp. 1000, 1992.

[88] H. Kohlmann, B. Bertheville, T. Hansen, and K. Yvon, "High-pressure synthesis of novel europium magnesium hydrides," *Journal of Alloys and Compounds,* vol. 322, pp. 59.

[89] R. J. Cava, A. W. Hewat, E. A. Hewat, B. Batlogg, M. Marezio, K. M. Rabe*, et al.*, "Structural anomalies, oxygen ordering and superconductivity in oxygen deficient $Ba_2YCu_3O_x$," *Physica C: Superconductivity,* vol. 165, pp. 419.

[90] D. E. Cox and A. W. Sleight, "Crystal structure of $Ba_2Bi^{3+}Bi^{5+}O_6$," *Solid State Comm.,* vol. 19, pp. 969.

[91] B. T. M. Willis and C. J. Carlile, *Experimental neutron scattering*. Oxford; New York: Oxford University Press, 2009.

[92] H. Rietveld, "A profile refinement method for nuclear and magnetic structures," *Journal of Applied Crystallography,* vol. 2, pp. 65, 1969.

[93] L. B. McCusker, R. B. Von Dreele, D. E. Cox, D. Louer, and P. Scardi, "Rietveld refinement guidelines," *Journal of Applied Crystallography,* vol. 32, pp. 36, 1999.

[94] R. B. V. D. A C Larson, "General Structure Analysis System (GSAS)," *Los Alamos National Laboratory Report,* vol. LAUR pp. 86.

[95] R. Haynes, S. T. Norberg, S. G. Eriksson, M. A. H. Chowdhury, C. M. Goodway, G. D. Howells*, et al.*, "New high temperature gas flow cell developed at ISIS," *Journal of Physics: Conference Series,* vol. 251, p. 012090, Dec 16 2010.

[96] F. G. Kinyanjui, S. T. Norberg, I. Ahmed, S. G. Eriksson, and S. Hull, "In-situ conductivity and hydration studies of proton conductors using neutron powder diffraction," *Solid State Ionics,* vol. 225, pp. 312, 2012.

[97] T. E. Engin, A. V. Powell, R. Haynes, M. A. H. Chowdhury, C. M. Goodway, R. Done*, et al.*, "A high temperature cell for simultaneous electrical resistance and neutron diffraction measurements," *Review of Scientific Instruments,* vol. 79, p. 095104, Sep 2008.

[98] A. Nowick and A. Vaysleyb, "Isotope effect and proton hopping in high-temperature protonic conductors," *Solid State Ionics,* vol. 97, pp. 17, May 1997.

[99] H. Iwahara, T. Yajima, T. Hibino, K. Ozaki, and H. Suzuki, "Protonic Conduction in Calcium, Strontium and Barium Zirconates," *Solid State Ionics,* vol. 61, pp. 65, May 1993.

[100] S. Imashuku, T. Uda, Y. Nose, K. Kishida, S. Harada, H. Inui*, et al.*, "Improvement of Grain-Boundary Conductivity of Trivalent Cation-Doped Barium Zirconate Sintered at 1600°C by Co-doping Scandium and Yttrium," *Journal of The Electrochemical Society,* vol. 155, p. B581, 2008.

[101] H. Iwahara, "Proton Conduction in Sintered Oxides Based on $BaCeO_3$," *Journal of The Electrochemical Society,* vol. 135, p. 529, 1988.

[102] R. Mukundan, E. L. Brosha, S. A. Birdsell, A. L. Costello, F. H. Garzon, and R. S. Willms, "Tritium Conductivity and Isotope Effect in Proton-Conducting Perovskites," *Journal of The Electrochemical Society,* vol. 146, pp. 2184, 1999.

[103] W. Yanzhong, C. Anthony, B. Emile, and D. Guilhem, "Properties of Y-doped $BaSnO_3$ proton conductors," *Solid State Ionics,* vol. 214, 2012.

[104] Y. Wang, "Synthesis and characterisation of acceptor-doped $BaSnO_3$ compounds as proton conductors," Doctorate, SPMS - Laboratoire Structures, Propriétés et Modélisation des solides, Ecole Centrale Paris, Chine, 2009.

[105] E. Quarez, S. Noirault, M. Caldes, and O. Joubert, "Water incorporation and proton conductivity in titanium substituted barium indate," *Journal of Power Sources,* 2010.

[106] S. Norberg, I. Ahmed, S. Hull, D. Marrocchelli, and P. Madden, "Local structure and ionic conductivity in the $Zr_2Y_2O_7$-Y_3NbO_7 system," *Journal of physics. Condensed matter : an Institute of Physics journal,* vol. 21, p. 215401, 2009.

[107] D. Marrocchelli, P. A. Madden, S. T. Norberg, and S. Hull, "Structural Disorder in Doped Zirconias, Part II: Vacancy Ordering Effects and the Conductivity Maximum," *Chemistry of Materials,* vol. 23, pp. 1365, 2011.